SORBONNE UNIVERSITÉ

THESIS FOR THE HABILITATION
TO DIRECT RESEARCH

Mémoire pour l'obtention de l'Habilitation
à Diriger des Recherches

Interaction of geodesic acoustic modes and energetic particles in tokamak plasmas

Dr. Alessandro BIANCALANI

Max Planck Institute for Plasma Physics, 85748 Garching, Germany
biancalani@ipp.mpg.de

June 25th, 2019

Contents

a mia moglie Stéphanie

Chapter 1

Introduction: instabilities in tokamak plasmas

1.1 Tokamak plasmas

A plasma is an ionized gas, which can be found in nature (e.g. in planetary ionospheres, stellar coronas and interplanetary space) and recreated in the laboratory on Earth. Fusion plasmas are high temperature plasmas, heated with the aim of reaching self-sustained nuclear fusion. Nuclear fusion is based on the nuclear reaction transforming a few light nuclei into a heavier one with the net loss of mass and production of energy. In the sun, nuclear fusion of a hydrogen plasma confined by means of its own gravity, is the dominant process of production of energy, which then reaches our planet allowing life on Earth. In the laboratory, fusion plasmas are confined using magnetic fields (or alternatively, compressed and heated in very short times by means of lasers, in the so-called "inertial confinement fusion"). Amongst toroidal confinement devices, axisymmetric magnetic configurations named "tokamaks" are chosen for the results described in this dissertation (see Fig. 1.1). Tokamaks are easier to build and operate, and, to date, more performing than other confinement concepts such as stellarators or reversed-
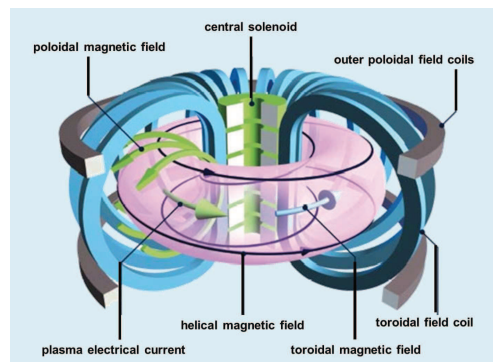

Figure 1.1: *A tokamak and its magnetic field (www.iter.org).*

field-pinches. The International Thermonuclear Experimental Reactor (ITER) is the result of an international collaboration and the expression of the effort in the scientific community to achieve the goal of operating in controlled burning plasma conditions [1], starting experiments in 2025.

Hot and dense plasmas must be produced to reach controlled nuclear fusion in tokamaks. Transport in tokamaks has been found to follow anomalous scalings with respect to Coulombian collision predictions. In particular, at the tokamak edge heat transport is found to be more than one order of magnitude higher than collisional transport for ions and three orders for electrons. Turbulent fluctuations in the electron density are observed mainly in the edge regions of tokamaks. Ion Temperature Gradient (ITG) modes and Trapped Electron Modes (TEM) are amongst the most common micro-instabilities responsible for turbulent transport in these devices, tapping the energy of the equilibrium temperature and density gradients (see Sec. 1.2.2). Numerical simulations have shown that this turbulence is fundamentally electromagnetic and nonlinear, i.e. not treatable with linear or secondary instability analysis [2]. Moreover, the heat transport can be largely enhanced by the presence of impurities in the tokamak plasmas.

It has been shown that time-dependent sheared flows can also be nonlinearly generated in a turbulent environment. These zonal flows (ZFs) - toroidally and poloidally symmetric structures - are important because they can contribute to the regulation of turbulence (see Sec. 1.2.1). Two types of ZFs have been observed in toroidal confined plasmas, i.e. a zero-frequency zonal flow (ZFZF) with a near zero frequency and a geodesic acoustic mode (GAM) with a higher frequency, of the order of the sound wave frequency. Recently, a number of experiments in several fusion plasma devices have shown the important role of ZFs in the LH transition (i.e. the transition from a "Low-confinement" tokamak mode, to a "High-confinement" tokamak mode, where the plasma confinement time is higher by a factor 2 or more), including both ZFZF and GAM.

Energetic ions in the MeV range are present in ignited plasmas, either as fusion products or because they are produced by auxiliary heating/current drive systems. Alfvén Eigenmodes are electromagnetic oscillations which propagate with the characteristic Alfvén velocity along the magnetic field lines (see Sec. 1.2.3). For typical tokamak plasmas, the Alfvén velocity is of the order of the thermal velocity of energetic ions. Therefore, Alfvén Eigenmodes can resonate with energetic ions and they are recognized as particularly dangerous due to their role in redistributing the energetic ion population, and therefore damaging the heating mechanism. Energetic ions can also make GAMs unstable, generating

energetic-particle-driven GAMs, i.e. EGAMs (see Sec. 1.2.1). EGAMs are also presently considered important for their role in redistributing energetic particles in phase space, and possibly interacting with turbulence.

1.2 Modes and instabilities in tokamaks

In this section, an introduction on modes and instabilities in laboratory plasmas is given. Reaching a complete theoretical understanding of these modes and instabilities is very important, due to their role in damaging the stability and confinement of heat and particles in fusion experiments. In particular, Geodesic Acoustic Modes, Zonal Flows, Ion-Temperature-Gradient modes and energetic-particle driven instabilities like shear Alfvén Eigenmodes and energetic-particle driven GAMs (EGAMs) are discussed here.

1.2.1 Geodesic Acoustic Modes and Zonal Flows

Geodesic Acoustic Modes (GAMs) [3, 4, 5, 6] and Zero-Frequency Zonal Flows (ZFZFs) [7, 8] are respectively low frequency ($\omega \sim c_s/R$, with c_s being the sound speed and R the tokamak major radius) and zero frequency ($\omega \ll c_s/R$) axisymmetric perturbation of tokamaks plasmas, with mainly m=0 (with m being the poloidal mode number) scalar potential component. Due to their key role in the turbulence saturation mechanism [9], understanding their formation and nonlinear interaction with turbulence modes is crucial for modeling and predicting transport properties of a tokamak plasma (see, for example, Fig. 1.2,
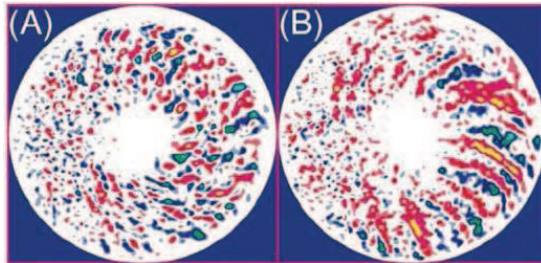
Figure 1.2: *Poloidal section of a tokamak turbulent plasma with zonal flows (A) and without ZF (B). Zonal flows break the turbulence vortices, substantially reducing the radial heat transport (from Ref. [10]).*

from Ref. [10]). At present day, the GAM frequency and spatial structure measured in tokamak plasmas are not well understood and predictable in terms of a theoretical framework, and a complete nonlinear global gyrokinetic investigation with a realistic tokamak geometry has not yet been performed. One main problem is the double nature of GAMs as contin-

uum modes and global eigenmodes. In fact, due to the fact that the GAM local frequency depends on the radial coordinate, phase mixing has been theoretically predicted to occur [4], and recently found in gyrokinetic simulations [11, 12, 13] (see Fig. 1.3). The characteristic signature of phase mixing, i.e. the linear growth of the radial wave-number in time in the presence of a temperature gradient, has also been studied in combination with the Landau damping, which depends on the spatial structure. When plasma parameters characteristic of realistic tokamak profiles have been considered, the GAM decay time has been found to be an order of magnitude lower than the decay due to the Landau damping alone, and in some cases of the same order of magnitude of the characteristic GAM drive time due to the nonlinear interaction with an ion-temperature-gradient (ITG) mode [11, 12, 13]. This has been proposed as the novel mechanism of damping, capable of explaining the disappearance of GAMs in the high-confinement tokamak mode (H-mode) where the temperature gradient at the edge are very high.

At the same time, GAMs with global structure have been observed in experiments. In the absence of energetic particles (EP), the main excitation mechanism of GAMs is the nonlinear interaction with ZFs and turbulence [9]. In this phase, it has been confirmed that the frequency radial profile of GAMs predicted theoretically using linear gyrokinetic simulations with experimental flux surface geometry and all species treated kinetically, does not well reproduce the value measured experimentally. The most likely reason has been conjectured to be the nonlinear interaction with turbulence [13].

Figure 1.3: *Wave-number of Geodesic Acoustic Modes (GAMs) increasing in time due to phase-mixing. The combined effect of phase mixing and Landau damping has been proposed as an explanation for the disappearance of GAMs observed in the high-confinement mode (H-mode) of tokamak discharges [11, 12, 13].*

When an EP population is present, zonal structures with frequency of the order of magnitude of the GAM frequency can also be excited via inverse Landau damping. These EP-driven GAMs, or EGAMs [14], can be important because of their nonlinear interaction with turbulence, and also because of their nonlinear redistribution of EP in phase space. A dedicated introduction to EGAMs is given in Chapter 2.
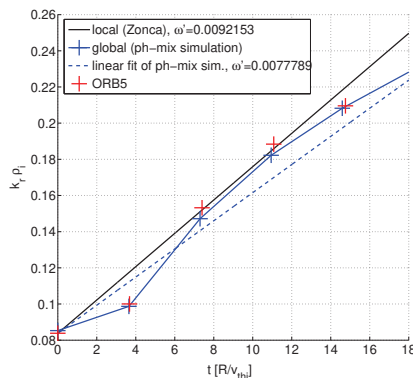
10

1.2.2 Micro-turbulence modes

Ion-temperature-gradient modes (ITG) [15] are drift-waves, driven unstable in tokamaks by ion temperature gradients. ITGs are, together with "trapped-electron-modes" and "kinetic ballooning modes", some of the most common microinstabilities causing turbulent transport in tokamaks. Extensive investigations of ITG and TEM turbulence by means of electrostatic gyrokinetic simulations have been performed in the last decades, and recently also the electromagnetic effects have started being investigated numerically [16, 17]. The evolution of the mode in time can be divided in a first transient phase, followed by a linear phase, where the perturbed fields grow exponentially. Linear and nonlinear properties of electromagnetic

Figure 1.4: *Global structure of the vector potential of ITG in electromagnetic simulations with ORB5 [17].*

ITG turbulence have been found different with respect to the results of electrostatic simulations with electrons treated adiabatically. This sheds light about the importance of treating properly the parallel component of electron motion for correctly understanding the ITG linear dynamics, and consequently ITG turbulence behavior.

The spatial structure of the mode has been investigated in electromagnetic simulations (see Fig. 1.4). At the low-field side of the tokamak ($\theta = 0$), the scalar potential has a well defined poloidal structure with one dominant poloidal mode number m, whereas at the high-field side ($\theta = \pi$), the characteristic ballooning behavior can be observed, where the mode loses the well defined poloidal structure and is described by the composition of several poloidal mode numbers. As for the parallel component of the vector potential, the structure reflects the scalar potential modulated by a sinusoidal $m = 1$ envelope, yielding very small intensity at $\theta = 0$ and $\theta = \pi$. Moreover, the spatial structure of the ITG modes is routinely investigated experimentally in tokamak experiments, for example with reflectometers. To bridge the gap between the experimental measurements and numerical simulations, synthetic diagnostics are used to post-process the numerical results (see Fig. 1.5). This makes the comparison more realistic.

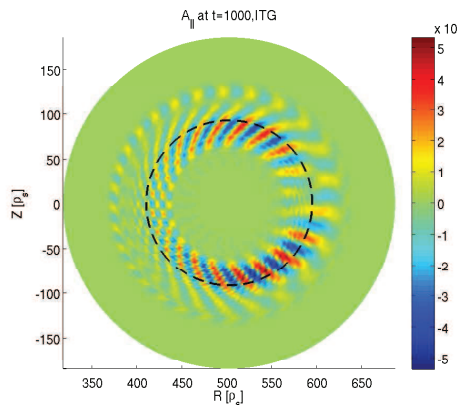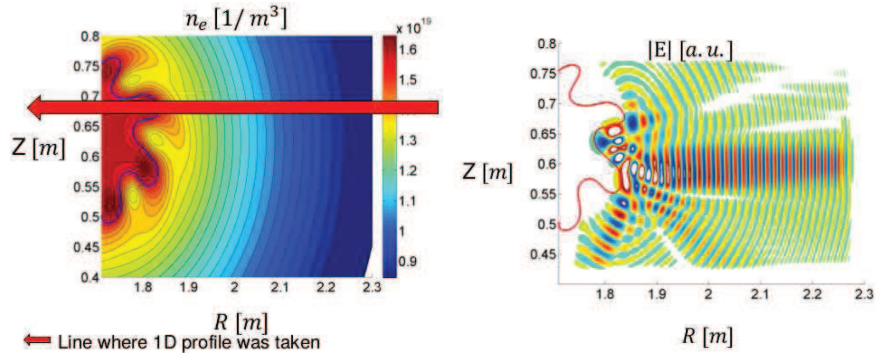Recently, the investigation of the nonlinear interaction of turbulence

Figure 1.5: *Electron density perturbation associated with the Ion-temperature-gradient (ITG) turbulence mode observed with ORB5 (left) and coupling of a synthetic full-wave reflectometer (right) [20].*

and global modes like Alfvén eigenmodes or EGAMs has started [18, 19]. The effect of turbulence on the mode saturation levels and the effect of the modes on the turbulent transport is being studied (see the next section for more details).

1.2.3 Shear Alfvén instabilities

Shear Alfvén waves (SAW) are transverse electromagnetic perturbations which propagate parallel to the ambient magnetic field with the characteristic Alfvén group velocity v_A. In fusion plasmas, fast ions in the MeV energy range have velocities comparable with the typical Alfvén speed and therefore these energetic particles (EP) can resonantly interact with SAW and effectively exchange energy with the wave [21]. SAW in a nonuniform equilibrium are subject to collisionless dissipation, known as continuum damping [22], due to singular structures that are formed where SAW continuum is resonantly excited. Due to magnetic field nonuniformities along the field lines in toroidal geometry, gaps appear in the SAW continuous spectrum [23] due to translational symmetry breaking, analogous to electrons traveling in a periodic lattice. Discrete Alfvén Eigenmodes (AE), with frequency inside SAW continuum gaps [24] have a generally low instability threshold, being affected only by Landau damping and practically unaffected by continuum damping. For this reason, understanding the continuous spectrum structure is important, due to the potential impact of AE stability on reaching the ignition condition for magnetically confined fusion plasmas.
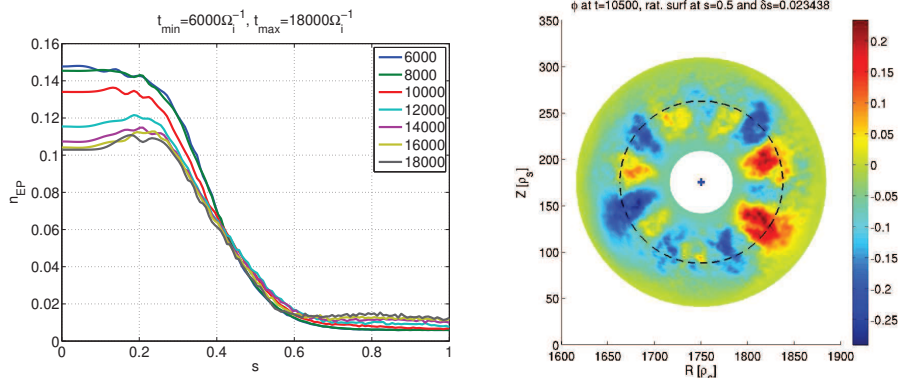
12

Figure 1.6: *Energetic particle radial redistribution at different times, for a nonlinear simulation where only one Alfvén mode is unstable (left) [25]. First investigations of coexistence of Alfvén modes and turbulence in electromagnetic simulations with ORB5 (right) [19].*

A) Gyrokinetic simulations of Shear Alfvén modes.

Due to non-negligible kinetic components of the SAW dynamics, such as Landau damping and resonances with EP, a gyrokinetic treatment is necessary if one wants to investigate properly the drive and damping mechanisms. For these reasons, gyrokinetic codes like ORB5, developed originally for turbulence simulations, have been developed for studies of Shear Alfvén modes.

The linear dynamics of Alfvén modes has been investigated with gyrokinetic codes, with detailed studies of the frequency and damping rates of axisymmetric SAW perturbations and of toroidicity-induced AE (TAE) (see fore example Ref. [26]). The nonlinear interaction of AE and EP has also been investigated with gyrokinetic codes, focusing on the study of the saturation mechanism. In particular, when EP are let redistribute due to the nonlinear wave-particle interaction (see Fig. 1.6), the characteristic scales of saturation levels vs linear growth rates can be measured (see for example Ref. [27, 28]).

Recently, the nonlinear interactions of AE and zonal structures and of AE and turbulence have also been investigated within a gyrokientic framework [25, 19]. Zonal structures such as GAMs and ZFZFs have been found to develop due to force-driven excitation during the AE linear phase.

B) Nonlinear interaction of Shear Alfvén modes and magnetic islands.

Although the first studies of AMs were carried out in axisymmetric

equilibria, in principle AMs can develop in any 3D shaped magnetic geometry, like for example in stellarator magnetic fields, or in tokamak magnetic fields modified by the presence of low-frequency MHD modes.

As an example of studies of AMs in nonlinear equilibria, the analytical theory of AMs in an equilibrium with a quasi-static magnetic island has been developed. The interest was born after the observation of modes in the beta-induced AE (BAE) [29, 30] frequency range in the Frascati Tokamak Upgrade (FTU) [31, 32] in the presence of an $(m, n) = (2,1)$ magnetic island, and in the absence of EP. Measured frequencies were found to depend on the magnetic island amplitude as well. The modes were observed only when the magnetic island size was over a certain critical threshold. Later on, similar observations have been reported in other tokamaks (e.g. in HL-2A [33]).

A novel analytical model has been developed to explain these observations, in the framework of a linear MHD theory for finite-beta tokamak plasmas [34] (see Fig. 1.7). When considering modes with different helicities from that of the magnetic island in the region inside the magnetic island, a SAW continuous spectrum, similar to that calculated in tokamak equilibria, has been found. A typical size magnetic island has been shown to have

Figure 1.7: *Beta-induced Alfvén eigenmode (BAE) and new magnetic-island-induced Alfvén eigenmodes (MiAE) [35, 36, 37].*

wide gaps in the continuous spectrum, due to the strong eccentricity of the flux surfaces, analogously to the formation of Ellipticity-induced AE gaps in tokamaks, but in this case inside the magnetic island equilibrium [35, 36]. When considering modes with the same helicity as the magnetic island, the BAE continuum accumulation point (BAE-CAP) has been found to be shifted in space from the rational surface of the island, to the separatrix flux surface position. The BAE-CAP frequency has also been found to be modified. Moreover, at the island O-point, several magnetic island induced CAP (MiO-CAP) have been found [37, 38, 39]. The existence of new magnetic-island-induced AE (MiAE), namely AE with a discrete frequency and a finite radial width inside the magnetic island, has also been discovered analytically [34]. The effect of the presence of X-points in the flux-surfaces on the AE dynamics is a crucial point here, and extrapolations to the dynamics of AEs in tokamaks with divertors, are straightforward.
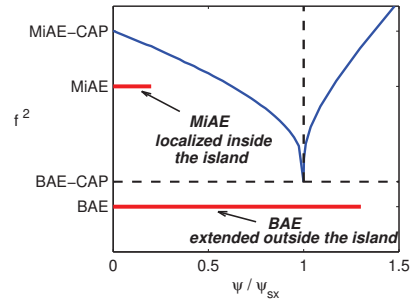
Chapter 2

The theoretical models

2.1 The role of GAMs and EGAMs in toka-mak plasmas

Zonal (i.e. axisymmetric) flows, associated to zonal structures of the radial electric fields, are often observed in turbulent tokamak plasmas, driven by the nonlinear interaction with drift-wave turbulence. Both zero-frequency zonal flows (ZFZF) [40, 7, 8] and finite frequency geodesic acoustic modes (GAM) [3, 4, 6] can be excited. GAMs have an oscillatory character, as they are basically a sound standing wave in the nonuniform tokamak magnetic field (the toroidal curvature being the main nonuniformity). GAMs are characterized by a dominant $m=0$ perturbed radial electric field and dominant $m=1$ perturbed density (m being the poloidal mode number). Due to their oscillatory character with frequencies of the order of the ion transit frequency, they are strongly affected by Landau damping (whereas ZFZF are mainly damped by collisional damping). As a consequence of this energy flow from microscopic to mesoscopic scales, ZFZFs and GAMs play a role as major turbulence saturation mechanisms. Moreover, in the presence of energetic particles (EP), EP-driven GAMs (EGAM) can be driven unstable due to inverse Landau damping. EGAMs have been studied theoretically [41, 14, 42, 43, 44, 45, 46, 47, 48, 49, 6] and experimentally (see for example Refs. [41, 50] and [51]). The role of EGAMs as possible mediators between EP and turbulence has also been emphasized [45, 48]. One of the main effects of EGAMs in tokamak plasmas is the redistribution of the EP population (crf. Ref. [52] for the implications on the losses of counter-passing EP). In particular, in phase space, this occurs due to nonlinear inverse Landau damping. As a possible consequence, EGAMs

might modify the efficiency of the heating mechanism of neutral beam injectors or ion cyclotron heating.

Understanding the dynamics of zonal structures like GAMs also sheds light on the physics of low-frequency Alfvén modes like beta-induced Alfvén Eigenmodes (BAE) [29]. This is due to the fact that GAMs and BAEs are degenerate in the long-wavelength limit, when diamagnetic effects are ignored [4]. In fact, both GAMs and Alfvén modes radially localized near a rational surface (i.e. where $k_\parallel = 0$), can be described by a vorticity equation derived from the quasineutrality, written in the following form [4, 43, 12]:

$$\frac{\partial}{\partial r}\Big(\frac{\partial^2}{\partial t^2} - \omega_c^2(r)\Big)\frac{\partial}{\partial r}\phi(r,t) = 0 \qquad (2.1)$$

The compressibility due to geodesic curvature coupling is identical for GAMs and BAEs, and determines the value of the local continuum frequency ω_c.

The radial structure of GAMs can be observed in tokamaks to be of a continuum type, or of a global type. Continuum GAMs are observed with a frequency which changes with the radial position due to the shapes of the plasma temperature profile and safety factor. On the other hand, a more global structure, like that peculiar of an eigenmode, is observed in some cases in tokamaks, and it is conjectured to be due to the nonlinear drive of the turbulence [13]. EGAMs show always a global structure, determined nonperturbatively by the EP profile (see for example Ref. [18], and the original prediction in Ref. [14]). Due to the non-existence of a radial structure of EGAMs in the absence of their drive, we define them as forced oscillations, analogously to the EPMs in the Alfvénic zoo [14, 21].

A kinetic model is necessary for theoretically describing GAMs and EGAMs. One reason is that the EGAM has a frequency of the order of magnitude of the sound frequency $\omega_s = \sqrt{2}c_s/R_0$, with $c_s = \sqrt{T_e/m_i}$ being the sound speed (with T_e the electron temperature and m_i the thermal ion mass) and R_0 being the major radius, and this is comparable to the transit frequency of thermal ions: therefore, resonances with the thermal ions substantially modify the EGAM frequency. Another reason is that the damping and excitation mechanisms, i.e. respectively the Landau damping and the inverse Landau damping, are intrinsically wave-particle mechanisms. Moreover, resonances with electrons are found to be important for a proper determination of the damping/growth rates of modes of the family of the GAM, and therefore, when a comparison of the theoretical predictions with experiments is desired, kinetic effects of electrons should also be retained [53, 13]. Due to the fact that numerical

16

simulations in 3D real space and 3D velocity space are numerically too demanding for the present computational capabilities, and include much physics which is not interacting with the EGAM due to separation of scales, it is desirable to reduce the model complexity.

Due to the fact that the EGAM frequency is much lower than the ion gyro-frequency, a reduction is possible from 6D to 5D in phase space, with the gyrokinetic (GK) model, averaging out the fast cyclotron motion. Within the same regime of low-frequencies, the magnetic moment μ can be considered as an invariant. Moreover, due to the axisymmetry of the EGAM perturbation, i.e. $n = 0$, we have that P_ϕ is also an invariant [14]. The adoption of a GK model for the numerical simulations strongly reduces the computational times. Nevertheless, a comparison with even more simplified reduced models is essential to identify the basic physics of the selected instability, and to push towards modeling techniques which can act in real-time, in parallel to a tokamak discharge. Such are 1D reduced models. The assumption of $\partial P_\phi / \partial t = 0$ helps us further reducing the EGAM dynamics to that of a nonuniform system with only one degree of freedom, i.e. the above-mentioned 1D reduced model. This is at the basis for the paradigm of the EGAM as 1-1 correspondence with the beam-plasma instability.

2.2 Main features of the GAM dynamics in MHD theory

The nonuniformity of the magnetic field, via the geodesic curvature, enters the dynamics of zonal (i.e. poloidally and toroidally uniform) electric field oscillations giving rise to geodesic acoustic modes (GAM). The simplest theoretical model to describe linear dynamics of GAMs is the ideal MHD model [3], which is helpful to derive the order of magnitude of the GAM frequency, but does not contain the physics of the wave-particle resonance, necessary for example to estimate the GAM damping rate and the EGAM growth rate. In this section, we adopt the ideal MHD model with uniform equilibrium pressure profile as a basic starting point to sketch the derivation of the dispersion relation and the energy channels of the GAM oscillation, with a didactic aim. The GAM energy channels have been described in details in several works, like for example in Ref. [54, 55, 56]. Here we just make a simple derivation which serves as starting point. Next, we aim to an extension to kinetic theory [30], where Landau damping is considered.

We start with the ideal magnetohydrodynamic (MHD) model. The three waves described by this model are the Shear Alfvén waves, the Fast Magnetosonic waves, and the Slow Magnetosonic waves (i.e. acoustic waves). We want to study modes with acoustic polarization, therefore we can neglect to the lowest order the magnetic perturbations (and associated current perturbations). Therefore, the model reduces to the momentum equation and the equation of state:

$$\varrho\frac{\partial \delta\boldsymbol{v}}{\partial t} = -\boldsymbol{\nabla}\delta p \qquad (2.2)$$

$$\frac{\partial \delta p}{\partial t} = -\Gamma P_0 \boldsymbol{\nabla}\cdot\delta\boldsymbol{v} \qquad (2.3)$$

Here ϱ is the mass density, $\delta\boldsymbol{v}$ the fluid velocity, and Γ the ratio of the specific heats. Here δp and P_0 are respectively the perturbed and equilibrium pressures, with P_0 assumed to be homogeneous for simplicity.

The perpendicular ExB velocity is excited in the so-called "Rosenbluth-Hinton test", by initializing a zonal (i.e. uniform in poloidal and toroidal directions) radial electric field, which is then let evolve in time. The magnetic field nonuniformity enters the dynamics via the geodesic curvature, giving the name to the geodesic acoustic mode. The perturbed ExB velocity is described in terms of the scalar potential as:

$$\delta\boldsymbol{v}_\perp = \frac{c}{B^2}\boldsymbol{B}\times\boldsymbol{\nabla}_\perp\delta\phi \qquad (2.4)$$

where, to lowest order, the scalar potential is zonal and therefore the perpendicular gradient reduces to a radial derivative.

We now rewrite here the model equations, Eqs. 2.2 and 2.3, after having applied the operator $\boldsymbol{\nabla}\cdot(\boldsymbol{B}/B^2\times...)$ to the momentum equation, Eq. 2.2. We obtain:

$$-\boldsymbol{\nabla}\cdot\left(\frac{\varrho c}{B^2}\frac{\partial}{\partial t}\boldsymbol{\nabla}_\perp\delta\phi\right) = -\boldsymbol{\nabla}\cdot\left(\frac{\boldsymbol{B}}{B^2}\times\boldsymbol{\nabla}\,\delta p\right) \qquad (2.5)$$

$$\frac{\partial \delta p}{\partial t} = -c\Gamma P_0\boldsymbol{\nabla}\cdot\left(\frac{\boldsymbol{B}}{B^2}\times\boldsymbol{\nabla}\,\delta\phi\right) \qquad (2.6)$$

In the following, we approximate B as uniform in the first term of Eq. 2.5, and commutate with the differential operator, using the hypothesis of small inverse aspect ratio ($\partial_r \sim r^{-1} \gg \partial_R \sim R^{-1}$) and neglecting higher order corrections in $\varepsilon = r/R$. On the other hand, the nonuniformity of B will be kept in both right-hand-side terms of Eqs. 2.5 and 2.6.

We now take the time-darivative of Eq. 2.5, and we use Eq. 2.6 for the time derivative of the pressure. The differential operator on the right

hand side of Eqs. 2.5 and 2.6 can be rewritten as $\boldsymbol{\nabla} \cdot B^{-2}\boldsymbol{B} \times \boldsymbol{\nabla} = B^{-2}(\boldsymbol{B} \times 2\boldsymbol{\kappa} + \mathcal{O}(B/qR)) \cdot \boldsymbol{\nabla}_\perp$, where $\boldsymbol{\kappa} = \boldsymbol{b} \cdot \boldsymbol{\nabla}\boldsymbol{b}$ is the curvature of the equilibrium magnetic field, $\boldsymbol{b} = \boldsymbol{B}/B$ being the unit vector. For the present derivation, we are interested in estimating only the order of magnitude of the GAM frequency, and therefore we retain only the curvature term (where the curvature can be approximated as $\boldsymbol{\kappa} \simeq \boldsymbol{R}/R^2$ by considering only the dominant contribute of the toroidal magnetic field) and we neglect the $1/q$ corrections. We obtain:

$$c\frac{\partial^2}{\partial t^2}\nabla_\perp^2 \delta\phi \simeq -\frac{\Gamma P_0}{\varrho}c\left[\left(\frac{\boldsymbol{B}}{B} \times 2\boldsymbol{\kappa}\right) \cdot \boldsymbol{\nabla}_\perp\right]^2 \delta\phi \qquad (2.7)$$

Due to the fact that the scalar potential is mainly zonal ($\boldsymbol{\nabla}_\perp = \hat{\boldsymbol{r}}\partial_r$ in Eq. 2.7), the only component of the curvature entering the dispersion relation is the *geodesic* component κ_s, defined as twice the poloidal component of the curvature $\boldsymbol{\kappa}$ in the plane tangent to the magnetic flux surface: $\kappa_s = \hat{\boldsymbol{r}} \cdot (\boldsymbol{b} \times 2\boldsymbol{\kappa}) \simeq 2\,\sin\theta/R$. Finally, by averaging on a magnetic flux surface, we obtain the natural frequency of oscillation of GAM:

$$\left(\frac{\partial^2}{\partial t^2} + \omega_{GAM}^2\right)\partial_r^2\overline{\delta\phi} = 0 \qquad (2.8)$$

where only the zonal component of the scalar potential $\overline{\delta\phi}$ is considered at the leading order, and the GAM frequency is given by:

$$\omega_{GAM} = \sqrt{\frac{\Gamma P_0}{\varrho}}\sqrt{\langle\kappa_s^2\rangle} = \sqrt{2}\,\frac{c_s}{R} \qquad (2.9)$$

with $\langle\kappa_s^2\rangle = \langle 4\sin^2\theta/R^2\rangle = 2/R^2$, with $\langle...\rangle$ being the flux-surface-average operator. This dispersion relation gives the order of magnitude of the GAM oscillation. Here an equation of state has been adopted in our fluid model, whereas a kinetic theory would provide the GAM frequency without dependence on this choice. Moreover, the wave-particle resonances are neglected here and can be considered only in the framework of a kinetic theory, giving quantitative modification to the real part of the frequency and allowing us to estimate also the collisionless (Landau) GAM damping rate and (inverse-Landau) EGAM growth rate, which are strictly kinetic effects.

We now multiply Eq. 2.5 with $\delta\phi$, and Eq. 2.6 with $p/(\Gamma P_0)$, to obtain the energy channels:

$$-\frac{\varrho}{B^2}c^2\delta\phi\frac{\partial}{\partial t}\nabla_\perp^2\delta\phi = -c\delta\phi\boldsymbol{\nabla} \cdot \left(\frac{\boldsymbol{B}}{B^2} \times \boldsymbol{\nabla}\,\delta p\right) \qquad (2.10)$$

$$\frac{1}{\Gamma P_0}\delta p\frac{\partial\delta p}{\partial t} = -c\delta p\boldsymbol{\nabla} \cdot \left(\frac{\boldsymbol{B}}{B^2} \times \boldsymbol{\nabla}\,\delta\phi\right) \qquad (2.11)$$

19

Summing up the two equations, and using the vector identity $f\boldsymbol{\nabla}\cdot\boldsymbol{A} = \boldsymbol{\nabla}\cdot f\boldsymbol{A} - \boldsymbol{A}\cdot\boldsymbol{\nabla} f$, we obtain the energy theorem in its local form:

$$\frac{\partial}{\partial t}\big(\epsilon_k + \epsilon_p\big) = -\boldsymbol{\nabla}\cdot\left(\frac{\boldsymbol{B}}{B^2}\times\boldsymbol{\nabla}\,c\,\delta p\,\delta\phi\right) \tag{2.12}$$

where the kinetic and thermodynamic energy densities are given respectively by:

$$\epsilon_k = \frac{1}{2}\varrho\,\delta v_\perp^2\ ,\ \ \epsilon_p = \frac{1}{2}\frac{1}{\Gamma P_0}\delta p^2 \tag{2.13}$$

Here we have used $\int\delta\phi\nabla_\perp^2\delta\phi\,d^3r = \int|\nabla\delta\phi|^2 d^3r$. The energy theorem in its global form is obtained by integrating over the volume in real space:

$$\frac{\partial}{\partial t}\big(E_k + E_p\big) = 0 \tag{2.14}$$

where $E_k = \int\epsilon_k\,d^3r$, $E_p = \int\epsilon_p\,d^3r$. By defining $\boldsymbol{V} = (\boldsymbol{B}\times\boldsymbol{\nabla}\,c\,\delta p\,\delta\phi)/B^2$, we have that $\int\boldsymbol{dS}\cdot\boldsymbol{V}$ is totally zero if we take a magnetic flux surface as external boundary of integration (where $\delta\phi = 0$). Note that $\int\boldsymbol{dS}\cdot\boldsymbol{V}$ plays the role of Poynting flux here.

2.3 Main features of the GAM dynamics in kinetic theory

Here, we sketch a basic derivation of the GAM dispersion relation in gyrokinetic theory. Several simplifications are done here, and this serves only to show the structure of the calculation, which follows Ref. [4] (with analogies with Ref. [30], invoking the BAE/GAM degeneracy). For more complete derivations, the reader should refer for example to Ref. [57, 58, 4, 59, 6].

We consider here the electrostatic limit of the gyrokinetic model (i.e. we neglect the magnetic perturbations), for a homogeneous plasma (i.e. we assume that the equilibrium profiles have no gradients). The equilibrium distribution function for the species s is assumed to be Maxwellian. The perturbed particle distribution function is written as a sum of the adiabatic and non-adiabatic parts:

$$\delta f_s = -\frac{e_s}{T_s}F_{0s}\widetilde{\delta\phi}\ +\ \delta K_s e^{iL_{ks}} \tag{2.15}$$

where $\delta\phi = \overline{\delta\phi} + \widetilde{\delta\phi}$ is the perturbed scalar potential, written as the sum of the zonal (i.e. flux-surface averaged) and non-zonal (i.e. oscillatory on

a flux surface) components. Note that for GAMs, we have that $\overline{\delta\phi} \gg \widetilde{\delta\phi}$. Also, here $L_{ks} = (m_s c / e_s B)(\mathbf{k} \times \mathbf{B}) \cdot \mathbf{v}$.

The gyrokinetic (GK) equation in the drift-kinetic regime (i.e. neglecting finite-Larmor-radius/finit-orbit-width effects, i.e. setting $J_0 = 1$) is:

$$\left(\omega_{tr}\partial_l - i(\omega - \omega_d)\right)_s \delta K_s = -i\frac{F_0 e_s}{T_s}\omega\left(\widetilde{\delta\phi} + \left(\frac{\omega_d}{\omega}\right)_s \overline{\delta\phi}\right) \qquad (2.16)$$

where ∂_l is the parallel derivative, $\omega_{tr} = v_\parallel / qR$, and the drift frequency for radially localized modes is $\omega_{ds}(\theta) = \hat{\omega}_{ds}\,g(\theta)$, with: $\hat{\omega}_{ds} = (k_\perp m_s c / eBR)(v_\perp^2/2 + v_\parallel^2)$, $g(\theta) = \sin\theta$. The Bessel function of the zeroth order, $J_0 = J_0(k_\perp \rho_{Li})$, denotes the gyroaverage operator.

The quasi-neutrality (QN), is derived by equating the densities of the ions and the electrons, $\langle \delta f_i \rangle = \langle \delta f_e \rangle$, where the angular brackets denote the integration in velocity space. In its general form in the drift-kinetic regime, this equation is written as:

$$\left(1 + \frac{1}{\tau_e}\right)\widetilde{\delta\phi} = \frac{T_i}{n_0 e}\left(\langle \delta K_i \rangle - \langle \delta K_e \rangle\right) \qquad (2.17)$$

where $\tau_e = T_e/T_i$. Note that, up to here, ions and electrons have been treated equally, with no assumptions on the adiabaticity of the electrons. The vorticity equation, which can be derived from the QN equation, is:

$$\frac{\omega^2}{v_A^2}k_\perp^2 \delta\phi = \left\langle \sum_s \frac{4\pi e_s}{c^2}\omega\omega_{ds}\delta K_s \right\rangle \qquad (2.18)$$

Note that, in the derivation of the GAM dispersion relation, one needs the gyrokinetic equation, Eq. 2.16, and either the QN equation or the vorticity equation, which are equivalent for the derivation.

One of the first properties of GAMs we know from experiments and numerical simulations, is that they have nearly $m = 0$ electric field, which means $\widetilde{\delta\phi} \ll \overline{\delta\phi}$. Moreover, as GAMs are sound oscillations, the expansion of the GK equation is done with the smallness parameter ϵ which measures the ratio $\omega_{di}/\omega \propto k_r\rho_i$, i.e. the square root of the plasma temperature. To the zeroth order, i.e. for temperature going to zero, we predict no GAM oscillation of the distribution function, i.e. $\delta K_s^{(0)} = 0$. Therefore, the dynamics of the GAM is given by the resolution for the higher order component, $\delta K_s^{(1)}$.

For the electrons, having predicted already, by considerations on the physics of the GAMs, that $\delta K_e^{(0)} = 0$ for both components (zonal and

oscillatory), we now proceed with the oscillatory component of order $\mathcal{O}(1)$:

$$\omega_{tr,e}\partial_l\widetilde{\delta K_e}^{(1)} - i\omega\widetilde{\delta K_e}^{(0)} = 0 \;\;\Rightarrow\;\; \partial_l\widetilde{\delta K_e}^{(1)} = 0 \;\;\Rightarrow\;\; \delta K_e^{(1)} = 0 \quad (2.19)$$

In summary, the adiabaticity of the electrons is naturally described by the choice of the decomposition of the distribution function done in Eq. 2.15, and for the electrons reads:

$$\delta K_e = 0 \qquad (2.20)$$

As a consequence, the QN equation can be written as:

$$\left(1 + \frac{1}{\tau_e}\right)\widetilde{\delta\phi} = \frac{T_i}{n_0 e}\langle\delta K_i\rangle \qquad (2.21)$$

We now focus on the expansion of the GK equation of the ions. By taking the flux surface average of the gyrokinetic equation, we get:

$$\omega\overline{\delta K_i} = 0 \qquad (2.22)$$

to all orders. We also recall that $\delta K_i^{(0)} = 0$ for both components (zonal and oscillatory). Passing now to the next order, i.e. $\mathcal{O}(\epsilon)$, we have

$$\left(\omega_{tr,i}\partial_l - i\omega\right)\delta K_i^{(1)} = -i\frac{F_0 e}{T_i}\omega\left(\widetilde{\delta\phi}^{(1)} + \left(\frac{\omega_{d,i}}{\omega}\right)\overline{\delta\phi}^{(0)}\right) \qquad (2.23)$$

We now proceed to the resolution of Eq. 2.23 for $\delta K_i^{(1)}$. We write the flux-surface-averaged and oscillating fields in the following way: $\overline{\delta K_i}^{(1)} = \delta K_0$ ($= 0$) and $\widetilde{\delta K_i}^{(1)} = \delta K_c\cos\theta_0 + \delta K_s\sin\theta_0$, and a similar notation is used for $\delta\phi$. We get:

$$\begin{cases} \delta K_c = \dfrac{-iF_0 e\omega}{T(\omega^2 - \omega_{tr}^2)}\left(i\omega\delta\phi_c + \underline{\omega_{tr}\delta\phi_s} + \underline{\omega_{tr}\dfrac{\hat{\omega}_d}{\omega}\delta\phi_0}\right) \\[3mm] \delta K_s = \dfrac{-iF_0 e\omega}{T(\omega^2 - \omega_{tr}^2)}\left(-\underline{\omega_{tr}\delta\phi_c} + i\omega\delta\phi_s + i\hat{\omega}_d\delta\phi_0\right) \end{cases} \qquad (2.24)$$

This is the desired resolution of the GK equation of the ions. The next step, is to put δK into the QN. Before proceeding further, note that here, the underlined terms, are those which will be killed by the integration in velocity space, because odd (this assumes that F_0 is even, which is the case for the hypothesis of being a Maxwellian).

The last step of the derivation of the dispersion relation of GAMs is the resolution of the vorticity equation. Before doing this, we need to

write the oscillatory components of the scalar potential in terms of the zonal component. This is done by putting δK into the QN, which we also split into cosine and sine parts. We can then solve for $\delta\phi_c$ and $\delta\phi_s$ as a function of $\delta\phi_0$:

$$\begin{cases} \delta\phi_c = & 0 \\ \delta\phi_s = & \dfrac{I_2}{\left(1 + \frac{1}{\tau_e}\right) - I_1}\delta\phi_0 \end{cases} \qquad (2.25)$$

where I_1 and I_2 are the following integrals in velocity space:

$$I_1 = \int d^3v \frac{F_0}{\left(1 - \omega_{tr}^2/\omega^2\right)n_0} = -\zeta_{\|res}\mathcal{Z}(\zeta_{\|res}) \qquad (2.26)$$

and

$$I_2 = \int d^3v \frac{F_0}{\left(1 - \omega_{tr}^2/\omega^2\right)n_0}\frac{\hat{\omega}_d}{\omega} = -\frac{2k_\perp cT}{eBR}\frac{\zeta_{\|res}}{\omega}\left(\zeta_{\|res} + \left(\frac{1}{2} + \zeta_{\|res}^2\right)\mathcal{Z}(\zeta_{\|res})\right) \qquad (2.27)$$

where the integration in velocity space has been performed in cilyndrical coordinates $\int d^3v = 2\pi \int_0^\infty d\zeta_\perp \zeta_\perp \int_{-\infty}^\infty d\zeta_\|$, with $\zeta = v/v_t$, $v_t = \sqrt{2T/m}$, $\zeta_{\|res} = v_{\|res}/v_t$, $v_{\|res} = qR\omega$. We have also introduced the plasma dispersion function $\mathcal{Z}(z) = \pi^{-1/2}\int_{-\infty}^\infty e^{-y^2}/(y - z)dy$. This result can be cast in the following form:

$$\begin{cases} \delta\phi_c = & 0 \\ \delta\phi_s = & -\dfrac{2k_\perp cT}{eBR}\dfrac{1}{\omega}\dfrac{N(\omega/\omega_t)}{D(\omega/\omega_t)}\delta\phi_0 \end{cases} \qquad (2.28)$$

with $\omega_t = v_t/qR$, and:

$$\begin{cases} N(z) = & z + \left(\dfrac{1}{2} + z^2\right)\mathcal{Z}(z) \\ D(z) = & \dfrac{1}{z}\left(1 + \dfrac{1}{\tau_e}\right) + \mathcal{Z}(z) \end{cases} \qquad (2.29)$$

Note that the ordering of $\widetilde{\delta\phi}/\overline{\delta\phi}$ adopted, is verified here a posteriori, as $\delta\phi_s$ satisfies $\delta\phi_s/\delta\phi_0 \propto k_r T/(R\Omega_i\omega) \propto \omega_d/\omega$. Note also that, when the electron temperature vanishes, i.e. $\tau_e \to 0$, the GAM has a pure zonal electric field, i.e. $\delta\phi_s = 0$, because $D \to \infty$.

We are now ready to solve the vorticity equation. This is taken at the first order, and a flux-surface average is performed:

$$\frac{\omega^2}{v_A^2}k_\perp^2\delta\phi^{(0)} = \overline{\left\langle \frac{4\pi e}{c^2}\omega\omega_d(\theta)\delta K^{(1)}\right\rangle} = \left\langle \frac{2\pi e}{c^2}\omega\hat{\omega}_d\,\delta K_s^{(1)}\right\rangle \qquad (2.30)$$

When considering the several terms of $\delta K_s^{(1)}$ in Eq. 2.24, we note again the the the underlined terms are killed by integration in velocity space, because odd (again, we assume here F_0 being even). We obtain the following equation:

$$\frac{\omega^2}{\omega_t^2} + \frac{q^2}{4n_0}\Big(I_3 + I_4\Big) = 0 \tag{2.31}$$

where

$$I_3 = -\frac{8n_0}{\pi^{1/2}}\frac{N(\zeta_{\|res})}{D(\zeta_{\|res})}\int_0^\infty d\zeta_\perp \int_{-\infty}^\infty d\zeta_\| \, \zeta_\perp \frac{\exp(-\zeta_\|^2 - \zeta_\perp^2)}{\zeta_\|^2 - \zeta_{\|res}^2}\zeta_{\|res}^2\Big(\frac{\zeta_\perp^2}{2} + \zeta_\|^2\Big) =$$

$$= -4n_0\zeta_{\|res}\frac{N(\zeta_{\|res})^2}{D(\zeta_{\|res})} \tag{2.32}$$

and

$$I_4 = \frac{8n_0}{\pi^{1/2}}\int_0^\infty d\zeta_\perp \int_{-\infty}^\infty d\zeta_\| \, \zeta_\perp \frac{\exp(-\zeta_\|^2 - \zeta_\perp^2)}{\zeta_\|^2 - \zeta_{\|res}^2}\zeta_{\|res}^2\Big(\frac{\zeta_\perp^2}{2} + \zeta_\|^2\Big)^2 =$$

$$= 4n_0\zeta_{\|res}F(\zeta_{\|res}) \tag{2.33}$$

Finally, the result is the desired dispersion relation of GAMs, in implicit form in the complex plane [4] (see also Ref. [30] for the analogous derivation for low-frequencies Alfvén modes):

$$z + q^2\Big(F(z) - \frac{N^2(z)}{D(z)}\Big) = 0 \tag{2.34}$$

with $z = \omega/\omega_t$, and with F defined by:

$$F(z) = z\Big(z^2 + \frac{3}{2}\Big) + \Big(z^4 + z^2 + \frac{1}{2}\Big)\mathcal{Z}(z) \tag{2.35}$$

Note again that, in the limit of vanishing electron temperature, i.e. $\tau_e \to 0$, then the dispersion relation becomes $z + q^2 F(z) = 0$, because $D \to \infty$.

In the limit of moderate values of the safety factor q (typically $1.5 < q < 3$, for moderately low values of wavenumber), explicit formulas for the GAM frequency and growth rate can be obtained from Eq. 2.34 (see Ref. [58]):

$$\frac{\omega}{q\omega_t} = f_T^{1/2}\Big(1 + \frac{1}{q^2}\frac{f_{S1}}{f_T^2}\Big)^{1/2} \tag{2.36}$$

$$\frac{\gamma}{q\omega_t} = -\frac{\sqrt{\pi}}{2}q^3 f_T\Big[\exp(-x^2)\,(x^2 + 2\tau_e + 1)$$

$$+\frac{q^2}{4}k_r^2\rho_i^2\exp\Big(-\frac{x^2}{4}\Big)\Big(\frac{x^4}{128} + f_{S2}x^2 + f_{S3}\Big)\Big] \tag{2.37}$$

with $x = \omega/\omega_t = \Re(z)$, $\rho_i = \sqrt{2T_i/m_i}/\Omega_i$, $f_T = 7/4 + \tau_e$ and $f_{S1} = 23/8 + 2\tau_e + \tau_e^2/2$, $f_{S2} = (1 + \tau_e)/16$, and $f_{S3} = 3/8 + 7\tau_e/16 + 5\tau_e^2/32$ (with Ω_i being the ion cyclotron frequency).

2.4 The beam-plasma instability and the EGAM

In this dissertation, we investigate the linear dynamics of EGAMs due to inverse Landau damping and the nonlinear dynamics of EGAMs due to wave-particle nonlinearity. A strong analogy between the EGAM and the beam-plasma instability (BPI) [60, 61] exists (see [43, 62]). The BPI is basically a mono-dimensional (1D) problem, where the Langmuir wave is driven unstable by a beam of fast electrons. Although the Langmuir wave has a different physics with respect to sound waves, and lives in a higher frequency domain, nevertheless both the BPI and the EGAM are driven by a suprathermal species (fast ions for the EGAM, fast electrons for the BPI) via inverse Landau damping. Moreover, although the EGAM is a 2D problem in an equilibrium toroidal magnetic field, its excitation mechanism, i.e. the inverse Landau damping, acts mainly in one direction, namely the direction parallel to the local equilibrium magnetic field (although it should be noted that in a more complete model, an EGAM can be excited by any kind of nonuniformity in velocity, and not only in the parallel direction, but also in radial direction, and also by trapped particles). Therefore, once a proper mapping is made, both instabilities can be investigated in terms of an inverse Landau damping problem in a 1D system.

The basic properties of the EGAM linear excitation mechanism are those of the (inverse) Landau damping. It is worth to recall here the result of the Landau damping for the BPI problem, derived in the Vlasov-Poisson model. In this problem, the essential dynamics is that of the electrons, and the ions only act as a charged static background. Calling the plasma frequency ω_p and the wavenumber k, one obtains [60]:

$$\gamma_L = \frac{\pi}{2}\frac{\omega_p^3}{k^2}\frac{\partial f_0}{\partial v}\bigg|_{\omega/k} \qquad (2.38)$$

Note that, if the resonance velocity ω/k falls in a region where the derivative of the distribution function in velocity space is negative, Eq. 2.38 describes a damping. This is always the case if the equilibrium distribution function is a Maxwellian. On the other hand, if an energetic beam

is present, described as a shifted Maxwellian, then the situation can occur where the resonance velocity falls in a region where the derivative is positive. In this latter case, Eq. 2.38 describes a drive - this is the case analogous to the EGAM in tokamak plasmas. For a detailed derivation of the EGAM dispersion relation in gyrokinetic theory, the reader should see, for example, Ref. [14, 42, 43, 63, 64, 6].

In the EGAM system, the equilibrium magnetic field is not uniform but has a toroidal shape. In general, particles moving in a toroidal magnetic field can perform passing orbits, i.e. follow the magnetic field on both low-field side and high-field side, or perform banana orbits in the space restricted to the low-field side of the tokamak. By construction, in the EGAM problem considered here, the energetic ions are initialized with a bump-on-tail distribution function (beam distribution), with a relatively high parallel mean velocity along the equilibrium magnetic field, plus a smaller isotropic thermal distribution around the mean velocity. Due to the relatively high parallel velocity, the time derivative of their toroidal angle never vanishes (and therefore banana orbits of the EP in the low-field side are not considered in the present treatment). During their motion which is, to the leading order, directed along the equilibrium magnetic field, they perform small drifts towards higher values of the minor radius, and then towards lower values of the minor radius, known as the curvature and grad-B drifts. These drifts have zero time average: this defines orbits with an average radial position plus a radial orbit width.

The radial electric field of the EGAM can exchange energy with the energetic particles, due to their radial component of the trajectories, and in particular of the curvature drift [43]: $v_{dc} = (v_\parallel^2/\Omega_{EP})\mathbf{B} \times \nabla\mathbf{B}/B^2$. Due to the structure of the perturbed distribution function, the effective parallel wavenumber of the EGAM is $k_\parallel = 1/qR$, the phase-angle is $\Theta = \theta - \omega_{EGAM}t$ and its normalized time derivative is $\dot{\Theta}/\omega_{EGAM} = (v_\parallel - v_{\parallel r})/qR\,\omega_{EGAM}$. In terms of the phase angle, the energetic particles experience a periodic electric field, and their harmonic motion can be expressed as [43]:

$$\frac{\ddot{\Theta}}{\omega_{EGAM}^2} = -\frac{\omega_b^2}{\omega_{EGAM}^2}\sin\Theta \; , \qquad (2.39)$$

where ω_b is the bounce frequency of the energetic particles in the potential created by the wave. Using these considerations, the analogy with respect to the 1D beam-plasma instability (BPI) turns out to be evident. In fact, the BPI is described as given by a Langmuir wave, excited by a beam of energetic electrons along a given direction x. The Langmuir wave

has a perturbed electric field directed along x, oscillating at the plasma frequency $\omega_p = \sqrt{n_e e^2 / m_e \epsilon_0}$. Therefore, for both the EGAM and the BPI, the linear and nonlinear dynamics is determined by the motion of the energetic particles in the perturbed field, which is essentially a 1D motion.

2.5 From the linear to the nonlinear dynamics

While GAMs are observed in tokamaks plasmas because they are nonlinearly driven by turbulence, EGAMs are driven unstable by the nonuniformity of the EP distribution function in velocity space, due to inverse Landau damping. Therefore, EGAMs can be observed, if the linear EP drive is above a certain threshold, given by the balance with the Landau damping due to the thermal plasma. In the absence of EP, the dispersion relation shows the existence of an infinite number of zonal solutions oscillating with frequencies of the order of the sound frequency. One of them, the least damped, is the GAM, and the other ones are more strongly damped, and they are called Landau poles, originating as solutions of the plasma dispersion function. In different regimes, the addition of EP can drive an EGAM unstable starting from a GAM, or from a Landau pole, depending on how the resonances are matched (see Ref. [14, 64]).

In tokamak plasmas, EGAMs can grow unstable due to the drive of EP, and can significantly affect the EP redistribution in phase space. The level of importance of this redistribution is proportional to the amplitude of the EGAM electric field. Although a linearly unstable EGAM grows exponentially, the effect of nonlinearities is to modify the dispersion relation and eventually to yield a saturation. Two main nonlinearities can be responsible of the saturation: wave-particle nonlinearity and wave-wave nonlinearity. Due to their nature of EP-driven instabilities, EGAMs, like the BPI, saturate primarily due to the wave-particle nonlinearity, i.e. due to the nonlinear inverse Landau damping. This means that, when reaching a
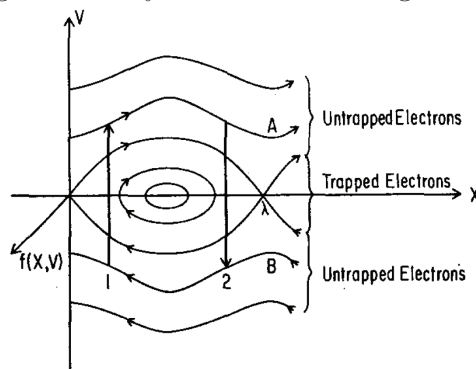

Figure 2.1: *Schematic representation of the phase space of electrons for the BPI problem (from Ref. [60]).*

27

certain amplitude, the EGAM electric field can displace the EP in the direction of the parallel velocity in phase space. Higher velocity particles lose energy, transmitting it to the EGAM field, and the effect is a flattening of the EP distribution function near the resonance. With respect to the potential wells created by the wave, the passing particles which lose energy can become trapped, and stop exchanging energy with the mode. A schematic picture of the island of passing and trapped particles is shown in Fig. 2.1, for the electrons responsible of the linear growth and nonlinear saturation of the BPI. Wave-wave nonlinearity can also occur for EGAMs, for example via generation of zero-frequency zonal flows, or of a second harmonic. In this case, the nonlinearity is predicted to be dominantly mediated by the EPs [65], rather then by thermal plasma nonlinearities.

Not only the linear dynamics, but also the nonlinear wave-particle dynamics has strong analogies for the two instabilities. In particular, the bounce frequency of the EP which fall trapped into the perturbed electric field is proportional to the square root of the perturbed electric field [43, 66], and the saturated electric field is proportional to the square of the linear growth rate [66, 67], as shown in Sec. 4.2. As a consequence, the question arises whether also the EP redistribution in phase space can be described with similar models for both instabilities. This will be discussed in Sec. 4.3.

The comparison of the nonlinear EP redistribution in velocity for the EGAM and the BPI is the problem faced in this dissertation. The BPI is studied here with a 1D code treating the thermal plasma as a cold dielectric medium and describing the dynamics of the fast electrons as an N-body problem solved with an Hamiltonian formulation [68, 69, 70]. A mapping of the velocity space for the EGAM system and for the bump-on-tail paradigm for the BPI is also formulated, allowing to find a one-to-one correspondence between EP redistribution studied in the two problems.

2.6 The numerical models

The choice of the model for the investigation of the dynamics of GAMs is dictated by their specific spatial and temporal characteristic scales. In particular, GAMs are zonal electric field oscillations (i.e. with toroidal and poloidal mode numbers equal to zero) with radial wavelength bigger than (or in same case of the order of) the ion Larmor radius, and time scales of the order of the sound time $\sim 2\pi R/c_s$. The basic physics is the one of the sound waves, therefore the MHD description is sufficient for

estimating the order of magnitude of the frequency of the mode [3]. Nevertheless, such spatio-temporal scales make the need of a kinetic treatment clear. This is due to the importance of resonances with passing ions, which can determine frequency and damping rate of the modes. Considering the requirements for the spatial scales, and the frequencies being lower than the ion cyclotron frequency, we can easily see that the gyrokinetic model [71, 72, 73, 74, 75, 76, 77] is the most appropriate tool.

ORB5 is a nonlinear gyrokinetic code based on a particle-in-cell (PIC) algorithm. The basic discretization scheme of a PIC code (also known as "Lagrangian" code), for the Vlasov-Maxwell problem, is presented in Ref. [78]. A PIC code discretizes the distribution function with macro-particles, also known as markers, associated with weights. In a gyrokinetic PIC code, the markers are pushed along the trajectories derived from the gyrokinetic model while the fields are known on a spatial grid and evolved by solving the gyrokinetic field equations either with finite differences or with finite element methods. The sources (charge density and current density) needed for solving the field equations are calculated by projecting the marker weights on a spatial grid. In ORB5, the distribution function is written as a sum of an analytical background distribution function and the perturbed distribution function, which is represented using markers via a control-variate Monte Carlo method, hystorically known as δf PIC [79] (see Ref. [88] for a recent overview).

ORB5 was originally developed for electrostatic turbulence studies [85]. In the last few years, it has been extended to the electromagnetic, multi-species version [16, 88]. In most of the results shown in this dissertation, we use the electrostatic version of ORB5 (except in Sec. 3.4.3, where the electromagnetic version of ORB5 is used), therefore we describe only the electrostatic model here. Only collisionless simulations are considered in this dissertation. No flux-tube version of ORB5 exists - only global ORB5 simulations are considered. The model equations of ORB5 are derived in a Lagrangian formulation [88], based on the gyrokinetic Vlasov-Maxwell equations of Sugama, Brizard and Hahm [76, 77].

The gyrocenter trajectories describe the motion of the markers of the kinetic species in phase-space coordinates written in $p_\parallel$-formalism, $\mathbf{Z}_{p_\parallel} = (\mathbf{R}, p_\parallel, \mu)$, i.e. respectively the gyrocenter position, canonical parallel momentum $p_\parallel = m_s v_\parallel$ and magnetic momentum $\mu = m_s v_\perp^2/(2B)$ (with m_s and q_s being the mass and charge of the species). $v_\parallel$ and $v_\perp$ are respectively the parallel and perpendicular component of the particle velocity. Note that here we describe the ORB5 model in the electrostatic limit (for the electromagnetic model of ORB5, the reader should

refer to Ref. [16]). The gyroaverage operator is labeled in this subsection by the tilde symbol $\tilde{\ }$. The gyroaverage operator reduces to the Bessel function J_0 if we transform into Fourier space. In all simulations with ORB5 shown in this dissertation, the gyroaverage is always calculated by considering non-vanishing Larmor radius for the ions, whereas it is calculated with zero argument for the electrons. In other words, finite-Larmor-radius (FLR) effects are retained for ions and neglected for electrons. The code ORB5 is based on straight-field-line tokamak coordinates. Dirichlet boundary conditions on the fields are imposed in the radial direction, while periodicity is assumed in the two angles. The nonlinear version of the trajectories is [88]:

$$\dot{\mathbf{R}} = \frac{1}{m_s} p_\parallel \frac{\mathbf{B}^*}{B_\parallel^*} + \frac{c}{q_s B_\parallel^*} \mathbf{b} \times \left[\mu \nabla B + q_s \nabla \tilde{\phi} \right] \qquad (2.40)$$

$$\dot{p}_\parallel = -\frac{\mathbf{B}^*}{B_\parallel^*} \cdot \left[\mu \nabla B + q_s \nabla \tilde{\phi} \right] \qquad (2.41)$$

$$\dot{\mu} = 0 \qquad (2.42)$$

Here, the time-dependent fields are the scalar potential ϕ and the parallel component of the vector potential $A_\parallel$, and $\mathbf{B}^* = \mathbf{B} + (c/q_s)\nabla \times (\mathbf{b}\, p_\parallel)$, where $\mathbf{B}$ and $\mathbf{b}$ are the equilibrium magnetic field and magnetic unitary vector. The linearization of this model is performed by pushing the markers along unperturbed trajectories:

$$\dot{\mathbf{R}} = \frac{p_\parallel}{m_s} \frac{\mathbf{B}^*}{B_\parallel^*} + \frac{c}{q_s B_\parallel^*} \mathbf{b} \times \mu \nabla B \qquad (2.43)$$

$$\dot{p}_\parallel = -\frac{\mathbf{B}^*}{B_\parallel^*} \cdot \mu \nabla B \qquad (2.44)$$

In this dissertation, the electrons are always treated with an "adiabatic" model except in Sec. 3.4.3 (where they are treated as drift-kinetic). In this "adiabatic" model, the electron gyrocenter density is calculated directly from the value of the scalar potential as [88]:

$$n_e(\mathbf{R}, t) = n_{e0} + \frac{q_s n_{e0}}{T_{e0}} \left(\phi - \bar{\phi} \right) \qquad (2.45)$$

where $\bar{\phi}$ is the flux-surface averaged potential. The quantities with subscript "0" refer to the equilibrium, and are functions of the radial coordinate ρ only.

The equation for solving the scalar potential is the gyrokinetic Poisson equation, also known as polarization equation. This is derived from the

gyrokinetic Lagrangian of ORB5, using the variational derivation, and imposing that the ExB drift energy of the particles is larger than the field energy (quasi-neutrality condition) [88]. The gyrokinetic Poisson equation is [88]:

$$ -\nabla \cdot \frac{n_0 m_i c^2}{B^2} \nabla_\perp \phi = \sum_s \int \mathrm{d}W \, q_s \, \delta \tilde{f}_s \qquad (2.46) $$

with $n_0 m_i$ being here the total plasma mass density (approximated as the ion mass density), and the summation over the species is performed when the electrons are treated as kinetic, otherwise the electron contribute is given by $-n_e(\mathbf{R}, t)$. Here $\delta f = f - f_0$ is the gyrocenter perturbed distribution function, with f and f_0 being the total and equilibrium (i.e. independent of time, assumed here to be a Maxwellian) gyrocenter distribution functions. The integrals are over the phase space volume, with $\mathrm{d}W = (2\pi/m_i^2) B_\parallel^* \mathrm{d}p_\parallel \mathrm{d}\mu$ being the velocity-space infinitesimal. The gyrokinetic Poisson equation is solved with a finite element method, by using B-splines in all the spatial directions.

Eqs 2.40, 2.41, 2.45, 2.46 are the constitutive equations of the model of ORB5 used in this dissertation for studying the collisionless dynamics of EGAMs. In the electromagnetic version, the Ampère equation is also solved for calculating the time evolution of the parallel component of the vector potential $A_\parallel$.

The Gyrokinetic Electromagnetic Numerical Experiment (GENE) code, is also a nonlinear gyrokinetic code originally developed for electromagnetic turbulence studies in the flux-tube (i.e. local) limit [80], recently extended to its global representation [93]. The model of GENE is also based on the gyrokinetic Vlasov-Maxwell equations of Brizard and Hahm [77]. Intra- and inter-species collisions (both pitch angle and energy scattering) are implemented. In this dissertation, only the linearized electrostatic collisionless version of GENE is used.

GENE is a Eulerian code. In a Eulerian description, the distribution function is not discretized with markers, but it is discretized on a 5D fixed grid in phase-space. The gyrokinetic equation is then solved on this grid for each species s. The coordinate system of GENE in the 5D phase space is written in $v_\parallel$-formalism, $\mathbf{Z}_{v_\parallel} = (\mathbf{R}, v_\parallel, \mu)$, i.e. respectively the gyrocenter position, parallel velocity and magnetic momentum.

As mentioned above, the linear physical models of ORB5 and GENE are equivalent, and no difference in the results is expected for the linear collisionless GAM/EGAM dynamics, depending on that. Nevertheless, the numerical schemes are different. Moreover, the existence of the two

representations of GENE, namely the global and the local (i.e. flux-tube) representations, offers the possibility to solve the model equations in two independent ways.

The GYrokinetic SEmiLAgrangian code (GYSELA) is also a nonlinear 5D gyrokinetic code [94]. The GYSELA code is dedicated to electrostatic Ion Temperature Gradient (ITG) turbulence with possibility to address transport of impurities (not treated here). Electrons have been assumed adiabatic in the previous versions, but a kinetic version has been recently developed and it is now in the test phase. GYSELA is a global full-f flux-driven code which addresses turbulent and neoclassical transports on an equal footing.

GYSELA is a global code with a toroidal geometry with a simplified concentric circular magnetic configuration. Its coordinate system in the 5D space is written as GENE in $v_\parallel$-formalism, $\mathbf{Z}_{v_\parallel} = (\mathbf{R}, v_\parallel, \mu)$ but where $R = (r, \theta, \varphi)$ with r the radial direction and θ and φ the poloidal and toroidal geometric angles. GYSELA is a full-f code, namely the back reaction of turbulent transport is accounted for in the time evolution of the equilibrium. In such a framework, the turbulence regime is evanescent if no free energy is injected in the system. A flux-driven version of the code is available since 2009 [87], where the system can be driven by a prescribed volumetric source, versatile enough to allow for separate injection of heat, parallel momentum and vorticity. However in this dissertation, the temperature and density profiles are constant and therefore we only use the forcing governed by the two equal thermal baths at the two radial boundaries. A linearized multi-species collision operator is implemented in the code [95] but here only collisionless simulations are considered.

The numerical scheme of GYSELA is based on a semi-Lagrangian method [96] (more specifically on a "backward semi-Lagrangian approach"), which is a mix between PIC and Eulerian methods exhibiting good properties of conservation [97]. In this method, the phase-space mesh grid is kept fixed in time (like in Eulerian codes) and the Vlasov equation is integrated along the trajectories (like in PIC codes) using the invariance of the distribution function along the trajectories (Liouville theorem). In GYSELA, the interpolation step is presently performed with cubic splines. Like for ORB5 and GENE, the model equations of GYSELA are based on the gyrokinetic equations of Brizard and Hahm [77].

In summary, the three numerical codes ORB5, GENE and GYSELA, adopt equivalent physical models. All these codes solve the ion dynamics based on the gyrokinetic equations (see for example Ref. [71, 72, 73, 74] for some early derivations, or Ref. [77] for a recent comprehensive review). On the other hand, these three codes solve the model equations in three

different ways: ORB5 [85, 16, 88] is Lagrangian (i.e. particle-in-cell), GENE [80, 93] is Eulerian, and GYSELA [97, 94] is semi-Lagrangian. Some of the differences in the physical models are the sources for the nonlinear simulations of turbulence, and the possibility of having elongated magnetic equilibria of ORB5 and GENE (whereas GYSELA assumes circular magnetic equilibria).

The importance of having a package of three codes with different solvers relies on the trustability achieved in the physical results. To this extent, linear and nonlinear simulations obtained with this package give a more rigorous basis for the physical interpretation, the comparison with the analytical theory, and the prediction of experimental measurements.

Chapter 3

Linear dynamics

In the previous chapter, the derivation of the basic features of GAMs and EGAMs has been sketched within the framework of the MHD and gyrokinetic theories. In this chapter, the linear dynamics of GAMs and EGAMs is studied numerically, and the results compared with the analytical predictions. This serves as a test for different numerical codes, which are supposed to recover the analytical scalings in the appropriate limits, in the process called "verification and benchmark". In this process, the limits of the different models are reveiled. For example, one can see that the numerical resolution in phase space of particle-in-cell codes like ORB5 (i.e. the number of markers approximating the distribution function) must be largely increased when the damping/growth rate of the mode is small, in order for the signal to be well visible on top of the statistical numerical noise. This process also serves for understanding better the regimes of validity of the different analytical formulas. We start with the description of the linear dynamics of GAMs, i.e. when no EP population is present, then we investigate the effect of EP, for a simplified case which will be used for the nonlinear studies, and for a case which is selected for the linear comparison with experiments.

3.1 Linear GAM dynamics

In this section, the linear dynamics of GAMs is investigated with the numerical codes ORB5, GENE and GYSELA, and compared with analytical formulas (the results shown here are taken from Ref. [81]). As described in the previous chapter, the physics of GAMs is the physics of acoustic eigenstates of a tokamak geometry. Therefore, the characteristic frequency is the sound frequency, proportional to the sound velocity

$c_s = \sqrt{T_e/m_i}$ and inversely proportional to the characteristic tokamak size R_0. On the other hand, it is more interesting to investigate the effect of second-order features of the magnetic field geometry. Here, we take as an example, the dependence on the safety factor q, describing the helicity of the magnetic field lines. As described in the previous section, this enters mainly as an estimate of the length of the field lines, and consequently of the time taken by the particles to complete an orbit in the direction parallel to the field lines (see Eqs. 2.36 and 2.37).

For the simulations shown in this section, we have considered an analytical equilibrium with concentric circular flux surfaces. We choose a tokamak equilibrium with high aspect ratio ($\varepsilon = a/R_0 = 0.1$), with $R_0 = 1.3$ m, $a = 0.13$ m. The value of the magnetic field on axis is $B_0 = 1.9$ T. Each simulation has a different flat q-profile. Flat temperature and density profiles are also always considered. The value of $\rho^* = \rho_s/a$ (with $\rho_s = c_s/\Omega_i$) is chosen as $\rho^* = 1/160$. A zonal (i.e. axisymmetric) radial electric field is initialized at t=0, then it is observed to oscillate in time, and damp due to Landau damping. The frequency is measured for different simulations with different value of q, obtained with ORB5, GENE and GYSELA, and it is found to scale correctly with the theoretical dispersion relation Zonca-1996 [30], and the explicit formula Sugama-2006 / Sugama-2008 [58], as shown in Fig. 3.1. In particular, note that the value of the frequency tends to $\omega_{q\to\infty}/q\omega_{ti} = 1.66$ for large values of q. Some minor differences are found at low values of q in the
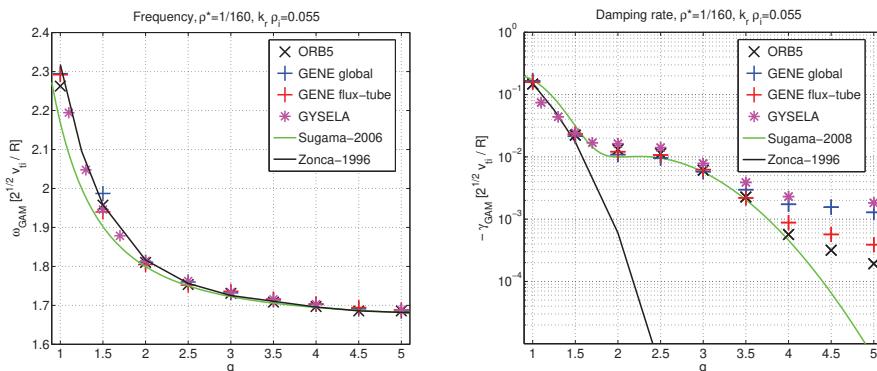

Figure 3.1: *Frequency (on the left) and damping rate (on the right), measured with ORB5 (Xs), GENE (crosses), and GYSELA (stars), and compared with the analytical formulas of Sugama-2006 / Sugama-2008 [58] (Eqs. 2.36 and 2.37, green lines) and Zonca-1996 / Zonca-2008 [30, 4] (Eq. 2.34, black lines) (from Ref. [81]).*

results of the dispersion relations (due to the hypothesis of large q considered by Sugama for the calculation of the explicit formula).

The dependence of the damping rate on q has also been studied, for the same simulations (see Fig. 3.1). All codes match well with the analytical predictions of Zonca-1996 at low values of q ($q \leq 1.5$). This is the regime where the orbits of the passing ions can be approximated as mainly directed along the magnetic field lines. For larger values of q, the passing ions experience orbits with a finite periodic motion in the radial direction. The radial width of their orbit becomes not negligible, and the modification of the resonant properties affects the dispersion relation (especially regarding the imaginary part of the frequency). Therefore, at larger values of q ($q > 1.5$), the finite-orbit-width (FOW) effects included at the first order in the explicit formula Sugama-2008 are shown to be dominant. All codes fit well with Sugama-2008 for values of q smaller than 3.5. At even larger values of q ($q \geq 3.5$) the higher-order FOW effects become dominant, and deviations from the formula Sugama-2008 are observed (see Ref. [81] for a dedicated discussion). The difference at large q between the flux-tube version of GENE (which agrees perfectly with ORB5) and the global version of GENE is due to the fact that the k_r used for global GENE runs was slightly larger. For this value of ρ^*, the choice of $k_r \rho_i = 0.055$ requires to simulate the entire domain in minor radius, while simulations of global GENE accounted only for 98% of it. This affects only the high q, i.e. when the damping is very small and the relative effect of k_r is large. Values of damping rates larger than ORB5 at large values of q are also observed with GYSELA, probably because the value of k_r has been observed to evolve in time towards values which are a bit larger than at the initial time of the simulations with GYSELA, and this increases the averaged damping rate.

As described in this section, the investigation of the linear properties of GAMs, like the frequency and damping rate, and the dependence on features of the equilibrium (like for example the magnetic field helicity given by the safety factor q, considered here as an example), shed light on the regimes of validity of the analytical theories and help understanding the behavior of the numerical codes. In the next section, a similar excercise is performed in the presence of energetic particles.

3.2   Linear EGAM dynamics

Here, we show results of GAMs with energetic particles described in Ref. [90]. The equilibrium profiles were originally chosen for simulations

performed with GYSELA [86, 87] and described in Ref. [63]. These are flat equilibrium temperature and density profiles and a nearly flat q profile. They are expected to behave as local simulations, due to the fact that the profiles are nearly flat. Results of electrostatic simulations are shown, with electrons treated adiabatically. In previous section, ORB5 has been successfully benchmarked on GAMs against analytical theory for linear simulations falling into this limit. In particular, in this report we show some first results of simulations with ORB5 where also an energetic particle population is present. At this step we consider with ORB5 a bump-on-tail EP population (see Ref. [63]). The dependence, in the linear phase, of frequency and growth/damping rates of GAMs and EGAMs on EP concentration is shown, and compared with results of GYSELA shown in Ref. [63].

We choose a tokamak equilibrium with circular flux surfaces and moderate aspect ratio ($R_0 = 1$ m, $\varepsilon = a/R_0 = 0.3125$), $B_0 = 1.9$ T, with flat equilibrium temperature and density profiles (we choose $\tau_i = T_i/T_e = 1$ and $\rho^* = \rho_s/a = 1/64$). Very low values of shear are considered at the center of the simulation box, where the measurements are done, so that the q profile is nearly constant with value $q = 3$, and our simulations are therefore expected to match local theory. The radial domain is chosen in the range $0.2 < \rho < 0.8$. In the inner half of the radial domain the value of the safety factor is always very near $q = 3$, with a maximum around $s = 0.25$ (s is the squared root of the poloidal magnetic flux, used here as radial coordinate). In the outer half of the radial domain, the safety factor increases to reach the value of $q = 3.25$ at the edge. Some simulations are also performed with flatter q profile and no difference in the results is observed. We initialize at $t = 0$ a charge density perturbation of the form $\sin(\pi r/a)$, which has a radial gradient but is independent of the poloidal and toroidal angle. In ORB5, a bump-on-tail distribution function for the EP population is implemented at the initialization of our simulations, $t = 0$, like in Eq. 27 of Ref. [63]:

$$F_{eq,h} = F_{M,h} e^{-\frac{\bar{\zeta}^2}{2\hat{T}_h}} \cosh\left(\frac{\bar{\zeta}\zeta}{\hat{T}_h}\right) \tag{3.1}$$

where $F_{M,h} = \frac{n_h}{(2\pi T_i \hat{T}_h/m)^{3/2}} e^{-\frac{\zeta^2 + 2\bar{\mu}}{2\hat{T}_h}}$. We choose the hot ion normalized temperature as $\hat{T}_h = T_h/T_i = 1$ and the normalized mean parallel velocity of hot ions as $\bar{\zeta} = v_\parallel/v_{ti} = 4$. The parallel velocity variable is $\zeta = \sqrt{2(E - \mu B)/m}/v_{th}$. The perturbation is let evolve in time with electrostatic simulation with adiabatic electrons.
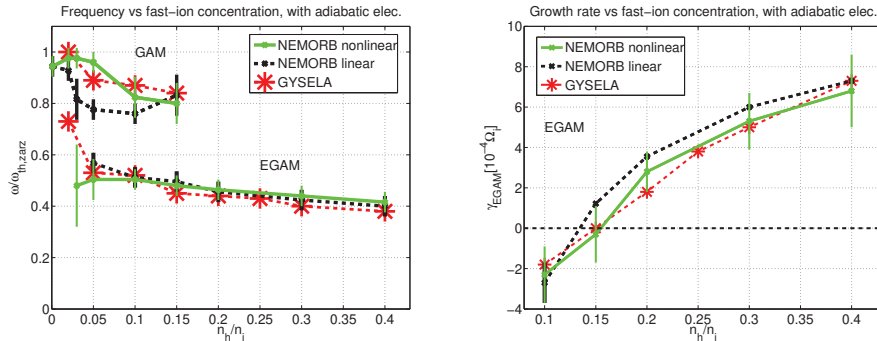
Figure 3.2: *Frequencies and growth rates of GAMs and EGAMs vs fast ion relative concentration, normalized with the theoretical value given in the absence of fast ions in Fig. 8,9 and 10 of Ref. [63], $\omega_{th,zarz} = 0.0125\,\Omega_i$. Green and black points are respectively nonlinear and linear results of ORB5 (a.k.a. NEMORB in 2014-2015), whereas red points are results obtained with GYSELA and described in Ref. [63] (from Ref. [81]).*

In a typical run we observe oscillations of $\mathrm{Im}(\phi_{10})$, which is the imaginary part of the complex Fourier transform in θ of the zonal component (n=0) of the scalar potential ϕ (in other words, $\mathrm{Im}(\phi_{10})$ is the Fourier coefficient of ϕ in θ relative to the $\sin(\theta)$ component). The typical period of the oscillations is of the order of the sound time $\tau_s \sim R/c_s$. We can observe the coexistence of two modes with different frequencies, where one is damped (GAMs) and one is growing (EGAMs). In the late phase we can observe a nonlinear saturation of the EGAM. In our simulations, we filter out all perturbations with toroidal mode number $n \neq 0$. Therefore, even though our simulations are nonlinear, no interaction with ITG or TEM turbulence is studied at this stage. The frequency of the modes is measured by performing a Fourier transform in time of $\mathrm{Im}(\phi_{10})$ at the mid radius, $s = 0.5$. Two main frequencies are detected: the higher frequency corresponds to GAMs and the lower to EGAMs. The growth rate of EGAMs is measured by performing a linear fit in logarithmic scale of the absolute value of $\mathrm{Im}(\phi_{10})$.

A scan of the frequency and growth rate of GAMs and EGAMs is shown in Fig. 3.2, vs the relative EP concentration n_h/n_i. Two set of simulations of ORB5 are shown: a set of nonlinear simulations, and a set of simulations performed with the linearized version of ORB5. In the nonlinear simulations, the trajectories are pushed using the Liouville theorem (see Ref. [90] for more details). We can see that results of nonlinear sim-

ulations performed with ORB5 agree with those of GYSELA described in Ref. [63]. GAMs are always damped and their frequency is difficult to measure for EP concentration higher than the EGAM instability threshold. On the other hand, we find EGAM frequency difficult to measure for EP concentration lower than $n_h/n_i = 0.05$. Regarding the growth rates of EGAMs, we observe a very good agreement of ORB5 nonlinear simulations with GYSELA, with an instability threshold at $n_h/n_i \simeq 0.15$ and an almost linear dependence on n_h/n_i. Slightly higher values of γ are found right above the threshold. Regarding simulations performed with linearized version of ORB5, we observe a general qualitative agreement with the nonlinear simulations, except for the frequency of GAMs, which is lower in linear simulations than in nonlinear simulations, and growth rates of EGAMs, which are higher in linear simulations than in nonlinear ones. This difference in the results is probably due to the fact that in the linear model we have chosen to initialize the EP distribution function as a function of constants of motion only, by neglecting the unperturbed terms in $d\zeta/dt$ in the Vlasov Equation. In the nonlinear model the initial distribution function is not an equilibrium and slowly evolves during the simulation. This could lead to the excitation of EGAMs for values of n_H slightly different from the ones in the linear simulation.

Next, we repeat a similar study as the one described above, with GENE and ORB5, studying the EGAM linear growth rates and frequencies for different fast particle concentrations in magnetic geometries with circular flux surfaces. These results are published by A. Di Siena in Ref. [49]. Electrons are considered adiabatic and at $t = 0$ a density perturbation of the form $n_1(s, t_0) \sim \sin(\pi s)$ is initialised and Dirichlet
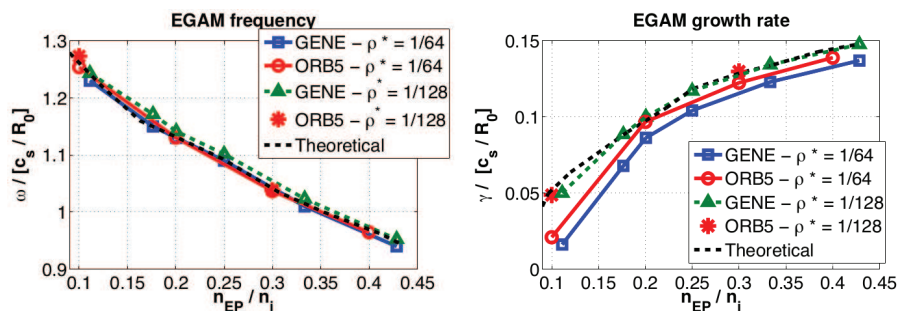

Figure 3.3: *Frequency (left) and growth rate (right) of EGAMs as a function of the EP concentration for a case with circular flux surfaces and q=3, obtained with GENE and ORB5 [49].*

boundary conditions are applied. Here, $s = \sqrt{\Psi_p/\Psi_{p,edge}}$ represents the radial coordinate with values in $[0, 1]$ and Ψ_p the poloidal flux. Both GENE and ORB5 consider the double bump-on-tail distribution function while a local Maxwellian is maintained for the main (thermal) ion species.

The considered magnetic equilibrium is the same as in the benchmark of ORB5 and GYSELA described above. Here, flat temperature and density profiles have been considered with the radial coordinate which goes from $0 < s < 1$. The EP and bulk ion temperatures ($T_e = T_i = T_{EP}$) are fixed by the choice of $\rho^* = \rho_s/a$. In the following two different values of ρ^* have been used, i.e. $\rho^* = 1/64$ and $\rho^* = 1/128$. The reference density, is a free parameter in collisionless electrostatic simulations as none of the physics inputs is constrained by this value and the chosen linear observables do not depend on the density either. Furthermore, the value of $\bar{v}_{\parallel}$, which determines the magnitude of the shift in $v_{\parallel}$, has been fixed to 2.83 in units of ion thermal velocity ($= 4$ in ORB5 units). In Fig. 3.3 EGAM growth rates and frequencies obtained for different energetic ion concentrations at $s = 0.5$ are compared between GENE and ORB5 for a flat q-profile $= 3$, i.e. shear $= 0$ and for $\rho^* = 1/64$ and $\rho^* = 1/128$. The theoretical values of the EGAM frequencies and growth rates have been taken from Ref. [64].

The differences between the GENE and ORB5 results are as the order of 7% for $\rho^* = 1/64$, which reduce to $\sim 5\%$ for ρ^*, i.e. $\rho^* = 1/128$. The agreement between the codes improves even further if the value of the flat q-profile is reduced to 2 (see Ref. [49]).

3.3 Case selection for nonlinear EGAM studies

3.3.1 Equilibrium and simulation parameters

We describe here the case selected for the nonlinear studies. This is well documented in Ref. [67]. The tokamak magnetic equilibrium is defined by a major and minor radii of $R_0 = 1$ m and $a = 0.3125$ m, a magnetic field on axis of $B_0 = 1.9$ T, a flat safety factor radial profile, with $q = 2$, and circular flux surfaces (with no Grad-Shafranov shift). Flat temperature and density profiles are considered at the equilibrium for all species. The bulk plasma temperature is defined by $\rho^* = \rho_s/a$, with $\rho_s = c_s/\Omega_i$, with $c_s = \sqrt{T_e/m_i}$ being the sound speed. Three increasing values of bulk plasma temperature are considered, for investigating the dependence of
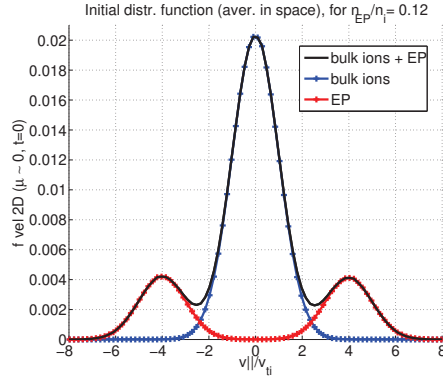
Figure 3.4: *Initial EP "double bump-on-tail" distribution function for a simulation with $n_{EP}/n_i = 0.12$, $v_{bump}/v_{ti} = 4$.*

our results on the Landau damping, corresponding to: $\rho_1^* = 1/256 = 0.0039$, $\rho_2^* = 1/128 = 0.0078$, and $\rho_3^* = 1/64 = 0.0156$ ($\tau_e = T_e/T_i = 1$ for all cases described in this dissertation).

All parameters defined so far, are adopted by ORB5 with no consideration of the mass of the bulk ion species. The choice of the bulk ion mass is done only during the post-processing of the results of ORB5, if we need to know the values of equilibrium or perturbed quantities in non-normalized units. In particular, in the case of a hydrogen plasma, we get a value of the ion cyclotron frequency of $\Omega_i = 1.82 \cdot 10^8 rad/s$. With this choice of bulk specie, we can calculate the plasma temperature and sound frequency. The three values of plasma temperature are $T_{i1} = 515$ eV, $T_{i2} = 2060$ eV, and $T_{i3} = 8240$ eV. The sound frequency is defined as $\omega_s = 2^{1/2} v_{ti}/R$ (with $v_{ti} = \sqrt{T_i/m_i}$, which for $\tau_e = 1$ reads $v_{ti} = c_s$). We obtain the following three values of the sound velocity: $c_{s1} = 2.22 \cdot 10^5$ m/s, $c_{s2} = 4.44 \cdot 10^5$ m/s, $c_{s1} = 8.88 \cdot 10^5$ m/s. These correspond to the following three values of the sound frequency: $\omega_{s1} = 3.14 \cdot 10^5$ rad/s, $\omega_{s2} = 6.28 \cdot 10^5$ rad/s, and $\omega_{s3} = 1.25 \cdot 10^6$ rad/s.

The energetic particle distribution function is a double bump-on-tail, with two bumps at $v_\parallel = \pm v_{bump}$ (see Fig. 3.4), like in Ref. [90]. In this dissertation, $v_{bump} = 4 v_{ti}$ is chosen. In order to initialize a distribution function which is function of constants of motion only, the modified variable $\tilde{v}_\parallel = \sqrt{2(E - \mu B_{max})/m}/v_{ti}$ is used instead of $v_\parallel = \sqrt{2(E - \mu B(r,\theta))/m}/v_{ti}$ (similarly to Ref. [63, 90, 64]). Neumann and Dirichlet boundary conditions are imposed to the scalar potential, respectively at the inner and outer boundaries, $s = 0$ and $s = 1$.

3.3.2 Linear dynamics

The linear dynamics of EGAMs in an equilibrium similar to the one considered in Sec. 3.3.1, has been investigated in Ref. [64] for a bulk plasma temperature given by $\rho^* = 1/64 = 0.0156$, by means of ORB5 simulations and analytical theory. Here, we show a scan on the EP concentration, similar to what was done in Ref. [64], but with three different values of bulk plasma temperature, corresponding to three different values of ρ^*, as described in Sec. 3.3.1. The linear dynamics of this case, shown here, is described in detail in Ref. [67], and is needed as a basis for studying the nonlinear evolution (which is treated in Chapter 4). The dependence of the linear dynamics (frequency and growth rate) on the EP concentration is shown in Fig. 3.5. Both the frequency and the growth rates are observed to follow the qualitative scalings as described in Ref. [90] and [64]. Note, in particular, that the growth rate does not grow linearly with n_{EP}.

The dependence of the frequency on the EP concentration is not observed to change with ρ^*. Regarding the growth rate, no change is observed when going from $\rho_3^* = 0.0039$ to $\rho_2^* = 0.0078$, meaning that the measured growth rate is basically given by the value of the drive, and the Landau damping here is negligible for the chosen values of EP concentration. On the other hand, when further increasing the temperature, and going to $\rho_1^* = 0.0156$, a smaller value of growth rate is measured, meaning a higher Landau damping. The transit resonance velocity of the EP can be calculated by knowing the EGAM frequency of a specific simulation. Considering a case with $n_{EP}/n_i = 0.12$ as an example, the frequency is
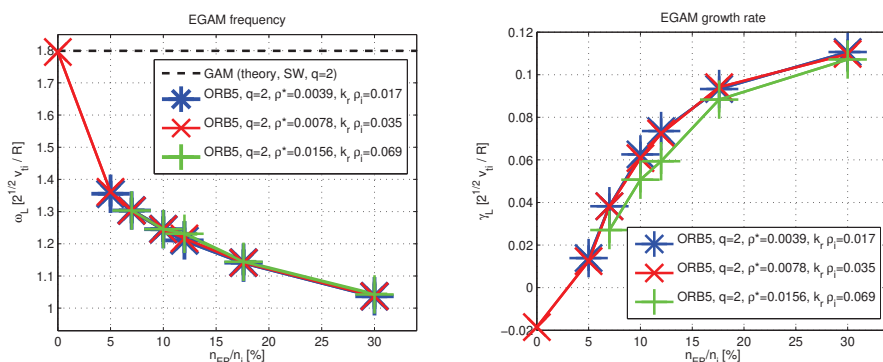

Figure 3.5: *Frequency (left) and growth rate (right) vs EP concentration, for simulations with $\bar{\zeta} = v_{bump}/v_{th} = 4$, $q=2$ [67].*

measured as: $\omega_L = 1.2\,\omega_s$. For comparison, the GAM frequency for these parameters is $\omega_{GAM} = 1.8\,\omega_s$. Then, the transit resonance velocity in the linear phase is calculated as $v_{\parallel 0} = qR\,\omega_L = 3.4\,v_{ti}$, with ω_L being the EGAM linear frequency.

3.4 Linear dynamics in experimental configurations

3.4.1 The reference case of ASDEX Upgrade

The AUG shot #31213 at time 0.84 s has been selected within the Non-Linear Energetic-particle Dynamics (NLED) Eurofusion enabling research project [98, 51]. It has been chosen to study the effect of the energetic particles (EPs) on the dynamics of EGAMs and Alfvén modes. In these simulations we have three species: gyro-kinetic thermal deuterium, gyro-kinetic energetic (fast) deuterium, and thermal electrons, either adiabatic (AE) or drift-kinetic (KE). The simulation with the AE
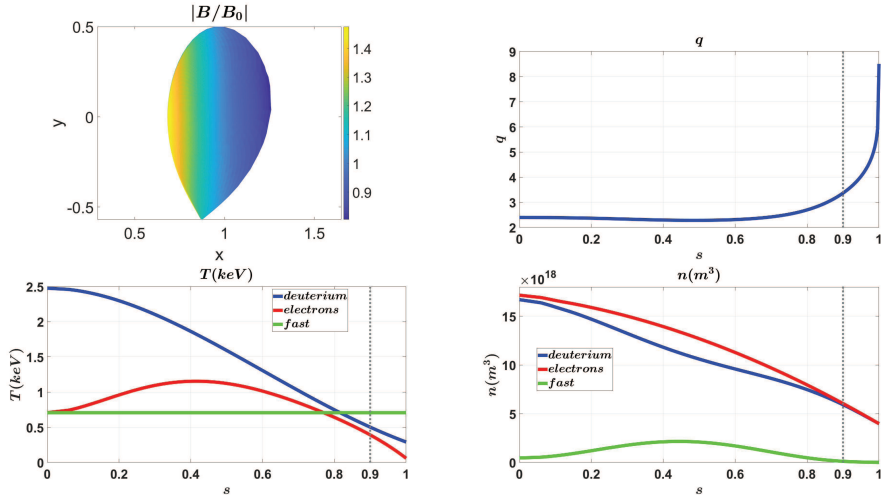

Figure 3.6: *Magnetic configuration (upper left plot), radial profile of the safety factor (upper right plot), species temperature (lower left plot) and density (lower right plot) radial profiles for the EGAM simulations in the NLED-AUG base case (ASDEX Upgrade shot #31213). The grey vertical dotted lines indicate the right boundary of the simulated radial domain in the EM case with drift-kinetic electrons [92].*

is performed in the electrostatic limit, while the simulation with the KE has been done including dynamics of the magnetic potential perturbation as well. In this latter case the pullback method [99] has been used for the mitigation of the cancellation problem in EM simulations [100, 101]. Corresponding profiles of the safety factor, species density and temperature are shown in Fig. 3.6. The magnetic field is reconstructed with experimental data, including all geometrical effects (Fig. 3.6). The magnetic field at the magnetic axis is $B_0 = 2.2$ T. The major radius at the axis is $R_0 = 1.67$ m. The geometrical major and minor radii are $R_0 = 1.62$ m, $a = 0.482$ m respectively. The magnetic equilibrium shape and the plasma profiles are shown in Fig. 3.6.

3.4.2   The effect of the flux surface elongation

As described in the previous sections, the dynamics of EGAMs is strongly determined by the drive given by the inverse Landau damping. Therefore, it is clear that a modification of the particle trajectories (given for example by a non-circular tokamak geometry) can yield a modification in the resonances, and therefore in the linear frequency and growth rates. In this section, our goal is to give a numerical estimation of the frequency and growth rate of EGAMs in the NLED-AUG case.

Before considering the experimental magnetic equilibrium of ASDEX Upgrade described in the previous section, we want to investigate here the effect of the elongation of the magnetic flux surfaces on the EGAM frequency and growth rate, by selecting a set of magnetic equilibria with different elongation. Simulations with adiabatic electrons are considered here. The results shown in this section are published by A. Di Siena in Ref. [49]. We consider the same physical parameters as in Sec. 3.2 and the value of ρ^* is fixed to $\rho^* = \rho_s/a = 1/128$. The q-profile is almost constant at the value of $q = 2$ in the whole range of the radial profile which goes from $0 < s < 1$ and the elongation is varied from $\kappa = 1$ (circular flux surfaces) to $\kappa = 1.75$. The fast ion concentration is $n_{EP}/n_e = 0.23$.

An excellent agreement is found with the codes GENE and ORB5. As a result, the EGAM growth rate is found to strongly decrease with the elongation (about a factor two for the considered range of values of the elongation), whereas the frequency decreases but more weakly (about 10% in the considered range). The decrease of the EGAM growth rate for elongated plasmas in weakly driven EGAMs is a direct consequence of the increase of the Landau damping due to the thermal ions (see the dedicated studies in Ref. [107, 108, 81]). This occurs because their transit frequency decreases for elongated plasmas, which pushes the resonance

towards the region of the distribution function with higher derivative in velocity space. A detailed study of this effect can be found in Ref. [49].

We now proceed to investigate the experimental magnetic equilibrium of ASDEX Upgrade described in the previous section and shown in Fig. 3.6. A first simplified setup with $T_i = T_e = 1.603$ keV, corresponding to $\rho^* = \rho_s/a = 1/183.3$ and considering flat temperature and density profiles is considered. These values have been taken from the full main-ion radial temperature profile at $s = 0.5$. For the nominal fast ion density $n_{EP} = 0.2\, n_e$ at $s = 0.5$, both codes agree well on the the values of the EGAM frequency and growth rate which are found to be $\omega = 1.267\, c_s/R_0 = 33.3$ kHz and $\gamma = 0.103\, c_s/R_0$ for the realistic AUG equilibrium. Fig. 3.8 furthermore demonstrates a pronounced effect of the magnetic geometry on the linear EGAM growth rates and frequencies. The plasma elongation is confirmed to weaken the EGAM growth rates and slightly reduce the mode frequency. A change in the EGAM fast ion density threshold can be observed as well. Consistently with the results shown above, the plasma elongation affects also the thermal damping, which unlike of the fast ion drive, strengthens with the elongation and can became dominant for the cases of weak EGAM drive. The combined effect of the elongation on the thermal damping and fast ion drive is found to significantly affect the fast ion density threshold.

We now consider simulations with the experimental plasma profiles described in Fig. 3.6. The corresponding EGAM growth rate and frequency are determined to $\gamma = 0.0465\, c_s/R_0$, $\omega = 2.013\, c_s/R_0 = 44.69$ kHz. Compared to values obtained for the case with flat profiles, the EGAM growth rate for these realistic AUG based parameters appears
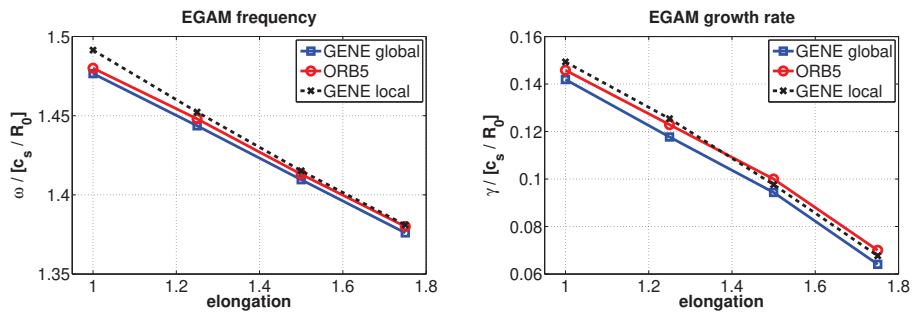

Figure 3.7: *Frequency (left) and growth rate (right) of EGAMs in dependence on the elongation, for a test case with $n_{EP}/n_e = 0.23$, $\rho^* = 1/128$ [49].*
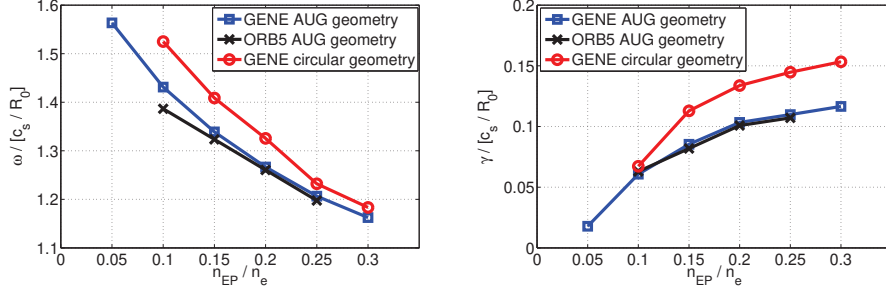
Figure 3.8: *Frequency (left) and growth rate (right) of EGAMs in dependence on the EP density, for the ASDEX Upgrade experimental equilibrium, with flat plasma profiles [49].*

to be relatively small. In the analysis discussed here, the NBI fast Deuterium temperature has been fixed to a realistic value of $T_{EP} = 30$ keV, which is calculated from the NBI injected energy while thermal NBI Deuterium had been considered in the simplified setup in the previous section. The aforementioned increase in the fast ion temperature produces a net reduction of the energy exchange term between fast ions and the mode with a consequent reduction of the EGAM growth rate. Furthermore, we also observe a significant increase in the EGAM mode frequency. It is also possible to compare the experimentally measured frequency of the $n = 0$ modes at $t = 0.841$ s and $s = 0.5$ with the values obtained by GENE with realistic density and temperature profiles. Despite the simplified setup here considered - adiabatic electrons, no nonlinear cou-
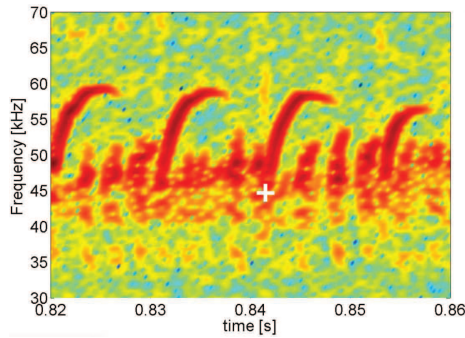

Figure 3.9: *Experimental spectrum of EGAMs in ASDEX Upgrade and theoretical prediction (white cross) [49].*

47

pling and electrostatic simulations - Fig. 3.9 displays a surprisingly good agreement between the measurement of the EGAM frequency in the first linear phase and the simulation value.

3.4.3 The effect of kinetic electrons

In this section, we show results obtained with ORB5 with simulations with adiabatic electrons (AE) and kinetic electrons (KE). The results shown in this section are published by I. Novikau in Ref. [92]. The simulations with the AE are performed with the electrostatic model, while the simulations with the KE have been done using the electromagnetic version of ORB5, i.e. including the dynamics of the magnetic potential perturbation. In this latter case the pullback method [99] has been used for the mitigation of the cancellation problem in EM simulations [100, 101].

In the EM case the radial domain has been reduced to $s = [0.0, 0.9]$ to avoid numerical instabilities due to the abrupt increase of the safety factor at the edge. The density profile, that is depicted in Fig. 3.6, corresponds to the case with $\beta_e = \langle n_e \rangle T_e/(B_0^2/(2\mu_0)) = 2.7 \cdot 10^{-4}$, where $\langle n_e \rangle$ is the electron density, averaged in a tokamak volume, μ_0 is the magnetic constant, and T_e is measured at the radial position $s = 0.0$. In both cases, the velocity distribution of the fast particles is described by the double bump-on-tail with $u_{H,f} = 8$ and $T_{H,f} = 1$. The ORB5 simulation with such parameters of the fast species results in one of the biggest EGAM growth rate for the given plasma configuration.

The Mode-Particle-Resonance (MPR) diagnostic [92], recently implemented in ORB5, provides the energy transfer signal $\mathcal{P}(v_\parallel, \mu, t)$ of the various species "sp" as a function of the velocity variables $(v_\parallel, \mu)$ and time, contributing to the total growth rate γ:

$$\gamma = \sum_{sp} \gamma_{sp} = -\frac{1}{2} Re \left[\left\langle \frac{\mathcal{P}}{\mathcal{E}} \right\rangle_t \right], \tag{3.2}$$

$$\mathcal{P} = \sum_{sp} \mathcal{P}_{sp} = \sum_{sp} \int \mathbf{J}_{sp} \cdot \mathbf{E} \, dV \tag{3.3}$$

Here $\mathcal{E}$ is the instantaneous mode energy, $\mathbf{J}_{sp}$ is the current carried by a species, and $\mathbf{E}$ is the radial perturbed electric field. By averaging this signal on several GAM/EGAM periods, resonances of the mode-particle interaction can be localised in the velocity space. Their location can be compared with the analytically given parallel resonance velocity:

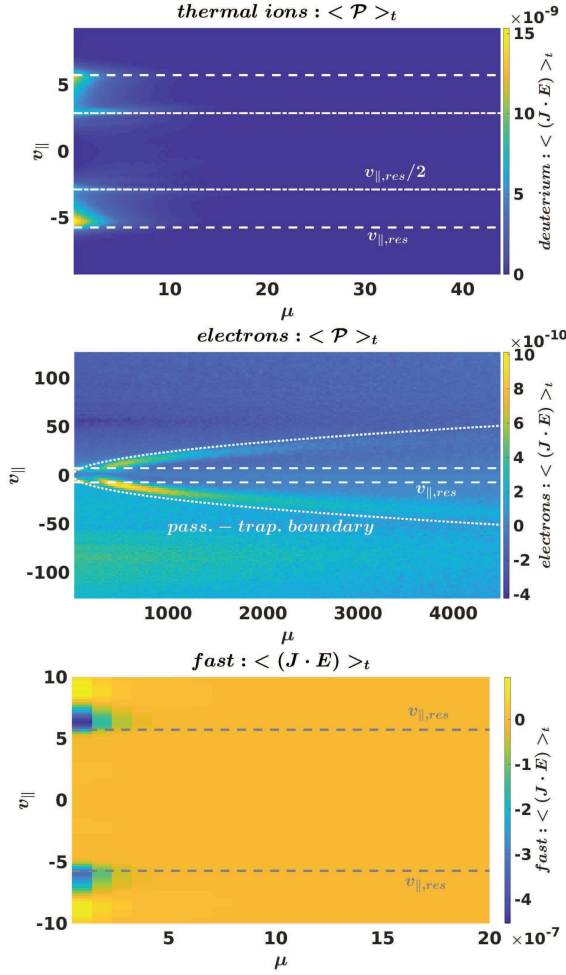$$v_{\parallel,res} = qR_0\omega_{GAM}, \tag{3.4}$$

Figure 3.10: *The energy transfer signal of EGAMs in the NLED-AUG case with the thermal ions (up), electrons (middle), and EP (bottom). The white dashed lines indicate the analytical estimation of the main EGAM-plasma resonance (Eq. 3.4). The dash-dot lines indicate position of the second resonance $v_{\parallel,res}/2$. The white cones indicate analytical estimation of the passing-trapped species boundaries [92].*

where ω_{GAM} is the GAM frequency, that can be found directly from the radial zonal electric field $\overline{E}_r$.

When applying the MPR diagnostic to simulations of EGAMs in the NLED-AUG case with AE (like those described in the previous section),

the total measured growth rate is:

$$\gamma_{AE}[\sqrt{2}v_{th,i}/R_0] = 1.62 \cdot 10^{-1} \pm 1.5 \cdot 10^{-3} \qquad (3.5)$$

consistent with the value measured by analysing the growth of the electric field in time.

We now repeat these simulations with KE. The first result to note is that the total growth rate, measured in the evolution of the radial electric field, is lower than in the case with AE. The reduction of the growth rate is not negligible, and for this simulation is estimated to about a factor 2:

$$\gamma_{KE}[\sqrt{2}v_{th,i}/R_0] = 8.4 \cdot 10^{-2} \pm 9.3 \cdot 10^{-3} \qquad (3.6)$$

We now apply the MPR diagnostic to understand which wave-particle interactions lead to the decrease of the EGAM total growth rate, by estimation of the contribution of different species. In the simulation with adiabatic electrons, the electrons do not contribute to the wave-particle resonances, so the contribution to the mode growth is given by the thermal ions and by the fast ions, in the following measure:

$$ions: \qquad \gamma_{AE,i}[\sqrt{2}v_{th,i}/R_0] = -2.99 \cdot 10^{-1} \pm 2.3 \cdot 10^{-3}, \qquad (3.7)$$
$$EP: \qquad \gamma_{AE,f}[\sqrt{2}v_{th,i}/R_0] = 4.62 \cdot 10^{-1} \pm 1.3 \cdot 10^{-3}. \qquad (3.8)$$

In case with drift-kinetic electrons, the species contributions are the following:

$$ions: \qquad \gamma_{KE,i}[\sqrt{2}v_{th,i}/R_0] = -3.8 \cdot 10^{-1} \pm 3.2 \cdot 10^{-2}, \quad (3.9)$$
$$electrons: \qquad \gamma_{KE,e}[\sqrt{2}v_{th,i}/R_0] = -3.0 \cdot 10^{-2} \pm 9.6 \cdot 10^{-4}, \quad (3.10)$$
$$EP: \qquad \gamma_{KE,f}[\sqrt{2}v_{th,i}/R_0] = 4.6 \cdot 10^{-1} \pm 4.1 \cdot 10^{-2}. \quad (3.11)$$
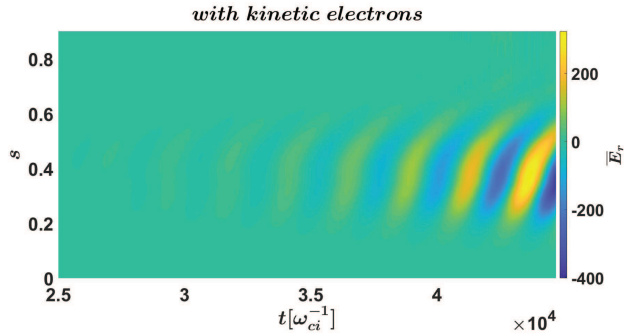

Figure 3.11: *Radial structure of EGAMs in the NLED-AUG case, obtained with ORB5 simulations with kinetic electrons [92].*

50

It is clearly shown here that in the experimentally relevant plasma conditions the inclusion of the drift-kinetic electrons significantly decreases the EGAM growth rate of about a factor 2. The reason is twofold: firstly, a non negligible electron Landau damping contributes to the total damping of the mode, and secondly, due to the slight modification of the mode structure and frequency, also the contribution of the two other species (thermal ions and EP) is slightly modified. For more details on the nature of these resonances and a discussion on the possible application of the MPR diagnostic, the reader should refer to Ref. [92].

The radial structure of the EGAM in the NLED-AUG case can also be studied with these linear simulations. The result for ORB5 simulations with kinetic electrons is shown in Fig. 3.11. The EGAM is shown to be radially peaked around $s \simeq 0.3$ and $s \simeq 0.4$. GENE also gives consistent results. For comparison, note that the mode observed in simulations with adiabatic electrons is found to be radially peaked at a larger radii ($s \simeq 0.5$).

Chapter 4

Nonlinear dynamics

4.1 The wave-particle nonlinearity

In this chapter, we describe the nonlinear evolution of EGAMs, and in particular the saturation level and the EP redistribution in phase space. By saturation level, we mean here the maximum level reached by the field right at the end of the linear phase, and before the amplitude starts decreasing. In the past, the nonlinear dynamics of EGAMs has been studied in various theoretical works (see for example Refs. [44, 63, 45, 47, 48]). As mentioned in Sec. 2.5, two possible types of nonlinear saturation are possible: wave-particle nonlinearity and wave-wave nonlinearity. The wave-particle nonlinearity is due to the redistribution of the EPs in phase space, and the wave-wave nonlinearity is due to the coupling of the EGAM field with other modes or with itself. In this dissertation, we focus on the wave-particle nonlinearity, and show how this saturation mechanism can be explained in terms of the inverse Landau damping, in comparison with the beam plasma instability (BPI).

The wave-particle nonlinear saturation has been studied with ORB5 with two main diagnostics: the measurement of the scaling of the saturation level with the linear drive, and the measurment of the redistribution of the EP population in phase space. For both, a key comparison is built with the nonlinear wave-particle saturation of the BPI. The scaling of the saturation level defines the regime of wave-particle interaction, and allows to build a predicting formula based on an analytical derivation. The study of the EP redistribution in phase space allows to investigate the effect of the EGAM field in modifying the EP distribution function around the resonance velocity.

The results presented in this chapter are described more in detail in

Ref. [67] and [103].

4.2 Nonlinear saturation level

4.2.1 Scaling of the saturated amplitudes

In this Section, we focus on the value of the saturated electric field $\delta \bar{E}_r$, and we investigate its dependence on the value of the linear growth rate and of the damping. The corresponding scaling of $\delta \bar{E}_r$ sheds light on the mechanism which is responsible for the saturation. A one-to-one comparison with the saturation mechanism of the BPI is also described.

The amplitude of the EGAM at saturation has been measured in different simulations performed with ORB5. The wave-particle nonlinearity only has been considered, by pushing on perturbed trajectories the EP population only. Therefore, even if the linear resonance velocity falls near the tail of the bulk ions (see Fig. 3.4), no nonlinear interaction of those bulk ions with the EGAM is considered in our model. More in general, the nonlinear interaction of the bulk ions with the EGAM is expected to be important: this has been studied in part analytically in Ref. [65], and its study with ORB5 is in progress. Different values of the bulk temperature, and the EP concentration, have been considered. As an example, the radial structure of a nonlinear simulation with $\rho^* = 0.0156$, $n_{EP}/n_i = 0.176$ is depicted in Fig. 4.1-a. No sensible change in the radial wave-number is observed when going from the linear phase, to the saturation, and after the saturation. This confirms that in this particular configuration, where all equilibrium radial profiles are flat, EGAM can be treated as a 1-dimensional problem where the radial direction does not play an important role.

When varying only the bulk temperature, both the linear frequency and growth rate are observed to scale with the sound frequency, which is a good normalization frequency (consistently with Fig. 3.5). The saturation level increases with the linear growth rate, similarly to other instabilities like the BPI in a uniform system and the Alfvén instabilities in tokamaks. This is depicted in Fig. 4.1-b, where non-normalized units are used (in particular, the ion cyclotron frequency is selected as a time unit not depending on the temperature).

The scalings with the energetic particle concentration are also investigated. The results are shown in Fig. 4.2a. We obtain that, in the considered regime, the saturated level scales as the quadratic power of the linear growth rate. This quadratic scaling is typical for marginally
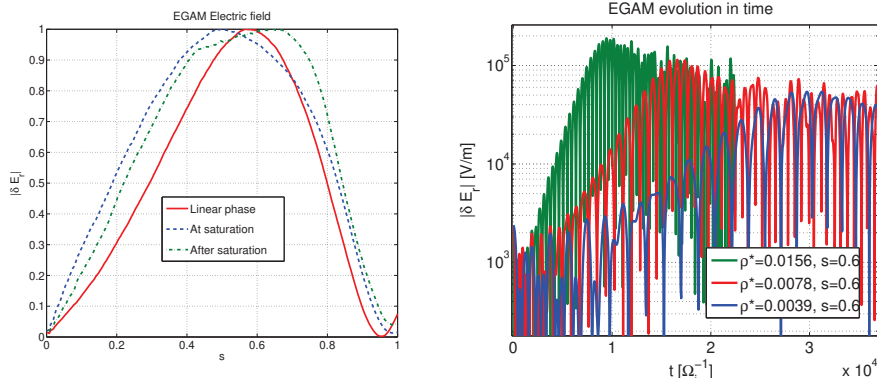
Figure 4.1: *On the left, EGAM normalized radial structure for $\rho^* = 0.0156$, $n_{EP}/n_i = 0.176$ during the linear phase (red, continuous), at saturation (blue, dashed), and after saturation (green, dash-dot). On the right, absolute value of the electric field measured at the position of the peak, $s = 0.6$, for three different simulations with respectively $\rho^* = 0.0039$ (blue), $\rho^* = 0.0078$ (red), $\rho^* = 0.0156$ (green). All simulations here have $n_{EP}/n_i = 0.30$. The time is expressed in units of Ω_i^{-1}.*

stable bump-on-tail instabilities, as derived by O'Neil [60, 61].

We can consider the problem to be similar to a monochromatic beam-plasma instability, in which particles are moving in the potential well of the perturbed electric field. Depending on the energy, some particles are trapped inside the well and execute bounce motion with frequency ω_b in the frame moving with the wave phase velocity. The resonant particles exchange energy with the mode, causing the amplitude to grow and the particles to redistribute in phase space, flattening the velocity distribution in the vicinity of the resonant parallel velocity $v_\parallel = \omega q R_0$. The drive is due to the positive slope of the particle distribution in the velocity space at the resonant parallel velocity, which acts as an inverse Landau damping. In the initial stage $\omega_b \ll \gamma_L$, the mode grows exponentially with a linear growth rate, making more and more particles to become trapped in the phase space. After some significant particle velocity redistribution, the power exchange between the wave and the particles is balanced, causing the wave amplitude to saturate.

Since the initial perturbation is negligible, the saturation level is determined by the exchange of energy between the mode and a band of resonant particles [66]. The chirping of the mode seen in Fig. 4.3 is a strongly non-linear effect that occurs when the amplitude is large enough

to have the trapped (and more generally resonant) particles with $\omega_b \sim \gamma_L$ drastically change the dynamics of the mode through the modification of the distribution function and non-perturbative fast particle response. Namely, the mode dynamics is determined by all resonant particles that exhibit a continuous oscillation, trapping and detrapping in the potential well of the mode, thus contributing (non-perturbatively) to the non-adiabatic behavior observed in the simulation.

The quadratic scaling of the saturation level with the damping obtained with our simulations is similar to the saturation of the BPI, where it occurs due to wave-particle trapping [60]. For the BPI, the original reference of M. B. Levin (1972) gives a value of $\omega_b = 3.06\,\gamma_L$ at saturation [66] (for comparison, note that more recent numerical calculations find $\omega_b = 3.2\,\gamma_L$ [102, 69]). For EGAMs, the bounce frequency (we use the units of the I.S. in this derivation) is given by [43]:

$$\omega_b^2 = \alpha_1 \, \delta\bar{E}_r \,, \quad \text{with } \alpha_1 \equiv \frac{e\hat{V}_{dc}}{2m_{EP}v_{\parallel 0}qR_0} \tag{4.1}$$

with m_{EP} being the mass of the energetic particle specie, considered equal to the bulk ion mass in this dissertation, $v_{\parallel 0}$ the velocity matching the resonance condition, and $\hat{V}_{dc} = m_{EP}v_{\parallel 0}^2/(eBR)$ the magnetic curvature drift. Therefore we have:

$$\alpha_1 = \frac{v_{\parallel 0}}{2qR^2B} = \frac{\omega_L}{2RB} \tag{4.2}$$

We emphasize that the value of α_1 depends on ω_L. This is a main difference with respect to the BPI, where there is only one value $\omega_{lin} = \omega_{pe}$ in the model, with ω_{pe} being the plasma frequency.

The dependence of the maximum electric field on the linear growth rate can be measured with the results of the numerical simulations. For the simulations shown in Fig. 4.2, we find:

$$\delta\bar{E}_r = \alpha_2\gamma_L^2 = \tilde{\alpha}_2\tilde{\gamma}_L^2 \tag{4.3}$$

where $\tilde{\gamma}_L$ is the linear growth rate normalized to the sound frequency ω_s, which is absorbed into the coefficient $\tilde{\alpha}_2$. The values of α_2 are found to depend on the bulk temperature. For the three chosen increasing values of ρ^*, i.e. $\rho^* = 0.0039$, 0.0078 and 0.0156, we have respectively $\tilde{\alpha}_2 = 0.47 \cdot 10^7$ V/m, $0.9 \cdot 10^7$ V/m, and $2.0 \cdot 10^7$ V/m. Finally the relationship between the EP bounce frequency and the linear growth rate is obtained:

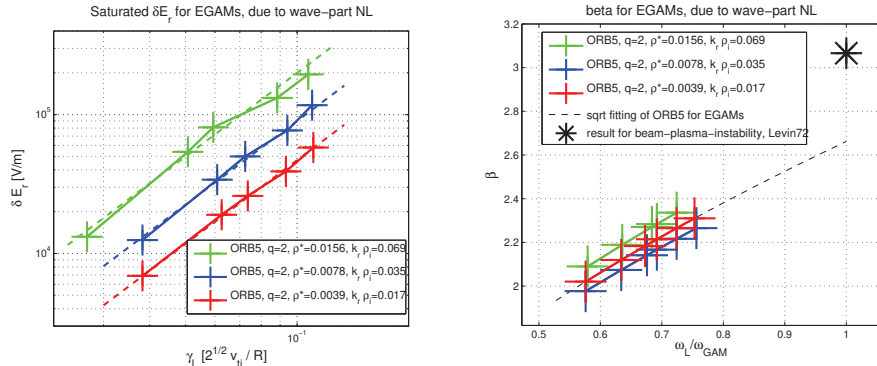$$\omega_b = \beta\,\gamma_L \tag{4.4}$$

56

Figure 4.2: *On the left, maximum value of the EGAM radial electric field, vs linear growth rate, for the same simulations as in Fig. 3.5. The red, blue and green crosses refer respectively to $\rho^* = 0.0039$, $\rho^* = 0.0078$, $\rho^* = 0.0156$. The dashed lines are the quadratic fitting formulas. On the right, the value of β as given in Eq. 4.5, vs the linear frequency, for the same simulations. The black dashed line is the sqruare root interpolation. For a reference, the black star shows the result obtained for the BPI in Ref. [66].*

where β is calculated as $\beta = (\alpha_1 \alpha_2)^{1/2} = (\alpha_1 \tilde{\alpha}_2)^{1/2}/\omega_s$, which yields:

$$\beta = \beta_0 \Big(\frac{\omega_L}{\omega_{GAM}}\Big)^{1/2}, \quad \text{with} \quad \beta_0 = \frac{1}{\omega_s}\Big(\frac{\omega_{GAM}\,\tilde{\alpha}_2}{2RB}\Big)^{1/2} \tag{4.5}$$

Note that here, β depends on the EGAM frequency, which changes with the intensity of the drive, given here by the EP concentration (see Fig. 3.5). As a comparison, note that in the problem of the BPI, solved in Ref. [60, 61, 66], on the other hand, the mode frequency is assumed to be constant and equal to the frequency measured in the absence of EP. On the other hand, the values of β are found not to depend on the damping, which changes with the three different bulk temperatures: an interpolation can be drawn for all considered simulations, and shown to depend on ω_L only (see Fig. 4.2b). In this sense, the formula given in Eq. 4.5 is universal for the chosen regime, because it does not depend on the bulk plasma temperature.

The considered equilibrium has been chosen in order to excite EGAMs out of a GAM, and not out of a Landau pole, as described in Ref. [64]. This choice of the mode is done, in order to have a one-to-one correspondence with the BPI, where the mode which is excited by the energetic electron beam is the Langmuir wave which is an eigenmode of the system

57

in the absence of EP. Following this consideration, we can consider the interpolation of the results shown in Fig. 4.2, and take the extrapolation to $\omega_L \to \omega_{GAM}$, which is the limit assumed in the resolution of the BPI. In this case, the extrapolation gives a unique value, which defines the EGAM instability, i.e. $\beta_0 = \beta(\omega_L/\omega_{GAM} = 1) = 2.66$. This is to be compared with the value of β obtained for the BPI [66, 102, 69], i.e. $\beta_{BPI} = 3.2$ (originally estimated as $\beta_{BPI} = 3.06$ by Levin).

Finally, by using Eqs. 4.1, 4.2, 4.4 and 4.5, we can write the formula for the saturated electric field as a function of the linear characteristics of the mode:

$$\delta E_r = \frac{2RB\beta_0^2}{\omega_{GAM}} \, \gamma_L^2 \tag{4.6}$$

with the value of $\beta_0 = 2.66$ in the regime considered in this dissertation.

4.2.2 Frequency

In this section, we show the results of the measurement of the time evolution of the EGAM frequency. In Sec. 4.2.1, we have shown that a quadratic scaling of the saturated electric field on the linear growth rate is found. This quadratic scaling, has a one-to-one correspondence on the Langmuir wave problem investigated by O'Neil, where the saturation occurs due to wave-particle trapping. The wave-particle trapping mechanism, is usually referred to as adiabatic, meaning that a slowly increasing potential well traps more and more energetic particles. In this adiabatic regime, the mode frequency varies very slowly with respect to the bounce frequency. On the other hand, in the EGAM case considered here, we show that the saturation is not strictly adiabatic, but a transition between adiabatic and non-adiabatic regime occurs at the time of the saturation.

In this section, we take again the EGAM case with $\rho^* = 0.0078$, $n_{EP}/n_i = 0.12$, as a typical case, and we investigate the variation of the frequency in time in comparison with the bounce frequency. For the measurement of the frequency, we use the radial zonal electric field measured at s=0.5. The measurement of the frequency is performed in two different ways: a) as an average of the period between several EGAM oscillation peaks, as shown in Fig. 4.3-a; b) with a short-time Fourier transform (STFT), as shown in Fig. 4.3-b.

With the first technique, namely measuring the frequency by inversion of the period between neighbouring peaks, an upward chirping is observed in the nonlinear phase, of the order of 10% of the linear frequency. This means that the resonance condition changes in time, with
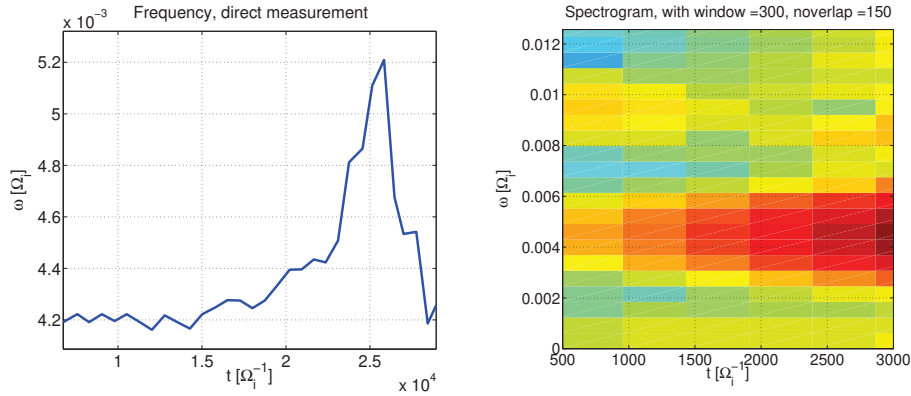
Figure 4.3: *Nonlinear evolution of the frequency, measured as a short-time average of the period between the peaks (left, "a") or with a short-time Fourier transform (right, "b"), for $\rho^* = 0.0078$, $n_{EP}/n_i = 0.12$.*

resonance velocity slightly increasing at the time of the saturation or in the later phase (see Fig. 4.3-a). A dominantly upward chirping of EGAMs was previously observed and documented in Ref. [41, 44]. In the cases of interest, the frequency changes with a similar time scale as the evolution of the amplitude. In this regime, we refer to this change of the frequency in time as nonlinear frequency shift, i.e. frequency chirping.

The second technique, consists in measuring the frequency with a short-time Fourier transform (STFT) on a Hamming time-window. With this technique, the error bar in frequency is large (due to the small number of oscillations in the nonlinear regime around the saturation), namely of the order of 10-20% (see Fig. 4.3-b). With such a big error-bar, no clear upward chirping is observed. Near the time of the saturation, i.e. $t \simeq 2.2 \, \Omega_i^{-1}$, only one mode is observed. This is the condition of application of the direct technique of measurement of the frequency described above, where the frequency can be measured as the inverse of the period among peaks.

As mentioned above, the EP bounce frequency ω_b depends on the mode amplitude. For this case, the mode amplitude grows during a linear phase, then enters the nonlinear phase and saturates at the time $t = 2.3 \cdot 10^4 \, \Omega_i^{-1}$. The corresponding value of ω_b^2 for the considered simulation is shown in Fig. 4.4-a. When the EGAM frequency evolves slowly in time with respect to the inverse of the bounce frequency, then the EP can bounce back and forth many times, and this is called adiabatic dynamics. The adiabaticity parameter, defined as ω'/ω_b^2, measures the
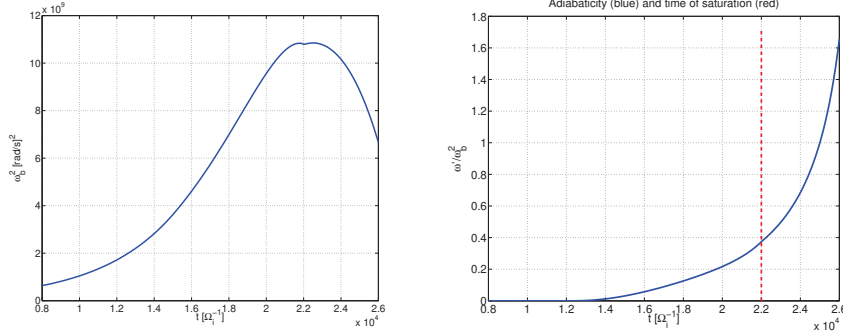
Figure 4.4: *Squared bounce frequency and adiabaticity for the EGAM with*
$\rho^* = 0.0078$, $n_{EP}/n_i = 0.12$.

level of adiabaticity of the dynamics. Here, ω' is the time derivative
of the frequency. The time evolution of the adiabaticiy parameter for
the considered simulation is depicted in Fig. 4.4-b (with ω being the
instantaneous mode frequency). A transition from adiabatic to non-
adiabatic dynamics near the saturation is observed. In particular, near
the saturation, the EP do not have the time to perform many bounces
during the nonlinear modification of the wave. From this respect, the
EGAM dynamics and the BPI are not in analogy.

4.3 Nonlinear transport in phase space

4.3.1 Nonlinear EGAM evolution

In this Section, we describe the evolution in time of the nonlinear simu-
lations of EGAMs performed with ORB5. Here, like in the rest of this
dissertation, the wave-particle nonlinearity only is considered. As an
example, we consider a case with $n_{EP}/n_i = 0.10$. A zonal (i.e. axisym-
metric) radial electric field is initialized at t=0, with an amplitude of the
order of 10^3 V/m, and let evolve in time in a nonlinear simulation with
ORB5. The results of the analysis of this case in phase space (described
in this Sec. 4.3) are taken from Ref. [103]. An initial linear phase is ob-
served, where the radial electric field grows exponentially in time. In this
phase the linear frequency and growth rate are measured and checked to
match with the ones of the linear simulation: $\omega_L = 1.24\,\omega_s$, $\gamma_L = 0.06\,\omega_s$.
Then, a nonlinear phase is entered, the growth rate gradually decreases
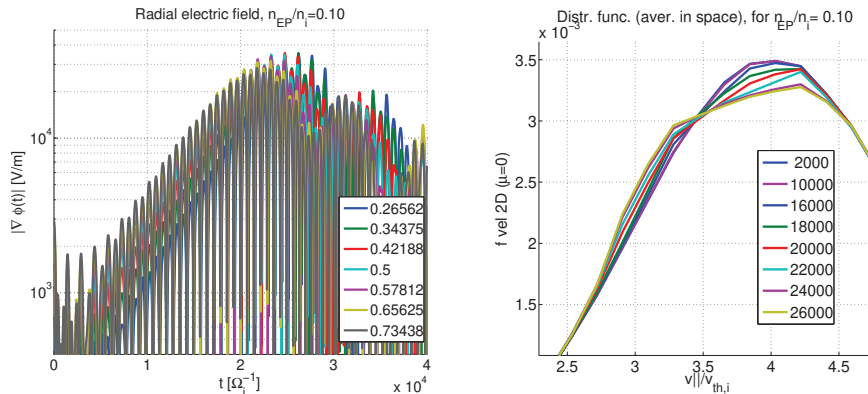to zero, and the radial electric field saturates at $t \simeq 2.5 \cdot 10^4\,\Omega_i^{-1}$ (see

Figure 4.5: *Radial electric field in time, at different radial positions (left), and EP distribution function at different times, vs parallel velocity (right) for an EGAM simulation with ORB5 with $n_{EP}/n_i = 0.10$.*

Fig. 4.5-a), when the electric field reaches a value of $\delta E_r \simeq 3.5 \cdot 10^4$ V/m. This value of the saturated electric field can be compared with the prediction derived in the previous Chapter (see also Ref. [67]):

$$\delta E_{r,th} = \frac{2RB\beta_0^2}{\omega_{GAM}}\,\gamma_L^2 = 3.5 \cdot 10^4 \frac{\text{V}}{\text{m}} \tag{4.7}$$

where the constant $\beta_0 = 2.66$ is estimated in Ref. [67] for this regime. For the present equilibrium plasma profiles, the regime is defined by the value of $q = 2$, for which we have an EGAM which comes from a GAM (see also Sec. 3.3.1). We emphasize here that the quadratic scaling of the electric field with the linear growth rate shown in Eq. 4.7 has been found to be valid for the whole considered range of EP concentrations (the same range used in Fig. 3.5). After the saturation, the EGAM enters a deep nonlinear phase ($t > 2.5 \cdot 10^4 \, \Omega_i^{-1}$), when the electric field starts decreasing in amplitude. In this dissertation we are interested in the first nonlinear phase only, up to the saturation, and we leave the study of the deep nonlinear phase to another dedicated article. In particular, we focus here on the nonlinear modification of the EP distribution function at the time of the saturation, and on the corresponding nonlinear modification of the EGAM frequency.

The EP distribution function redistributes in $v_\parallel$ during the first nonlinear phase, causing a relaxation of the drive due to the inverse Landau damping. The EP distribution function of this simulation is shown in Fig. 4.5-b). The redistribution of the EPs is observed to occur in a range
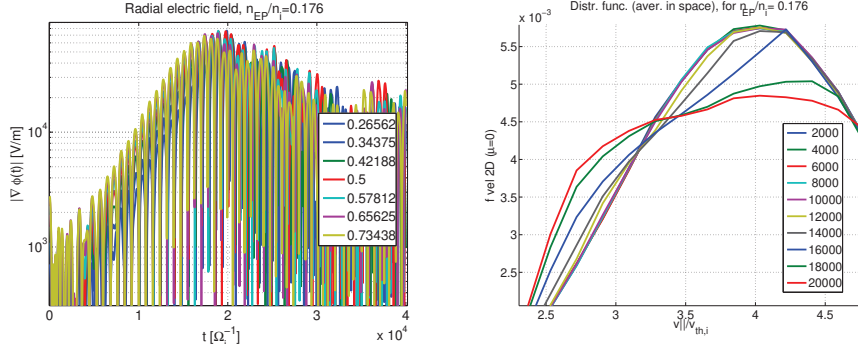
Figure 4.6: *Radial electric field in time, at different radial positions (left), and EP distribution function at different times, vs parallel velocity (right) for an EGAM simulation with ORB5 with $n_{EP}/n_i = 0.176$.*

of velocities between $2.5\,v_{ti}$ and $4.5\,v_{ti}$. The EP distribution function does not change during the linear phase, and when entering the nonlinear phase, the redistribution occurs with higher-velocity EP moving towards lower values of $v_\parallel$, as time increases. Therefore, negative values of the perturbed distribution function are measured at high velocities, and positive at low velocities. The resonance velocity can be calculated as $v_{\parallel res} = qR\,\omega_{EGAM} = 3.5\,v_{ti}$, and can be measured in Fig. 4.5-b as the velocity where the perturbed distribution function changes sign. We note that this velocity measured in Fig. 4.5-b, for this value of $n_{EP}/n_i = 0.10$, does not sensibly change in the time range of interest.

Before moving further, we want to consider another case for comparison, with a stronger drive, namely with $n_{EP}/n_i = 0.176$. The evolution in time of the radial electric field is shown in Fig. 4.6-a. The linear frequency and growth rate is measured and checked to match with the ones of the linear simulation: $\omega_L = 1.14\,\omega_s$, $\gamma_L = 0.094\,\omega_s$. The saturated level of the radial electric field is measured at $\delta E_r \simeq 0.8 \cdot 10^5$ V/m (in agreement with the prediction of Ref. [67]).

The EP distribution function of the case with $n_{EP}/n_i = 0.176$ is shown in Fig. 4.6-b, for different times up to the saturation. Firstly, we note that the range of velocities affected by the nonlinear modification is broader than that for the weaker drive. In fact, the redistribution of the EPs is observed to occur in a range of velocities between $2\,v_{ti}$ and $5\,v_{ti}$. Secondly, we note that the resonance frequency, which is calculated in this case from the linear frequency as $v_{\parallel res} = qR\,\omega_{EGAM} = 3.2\,v_{ti}$, does not perfectly describe the velocity of the change of sign of the perturbed distribution function at all times. In fact, the resonance velocity
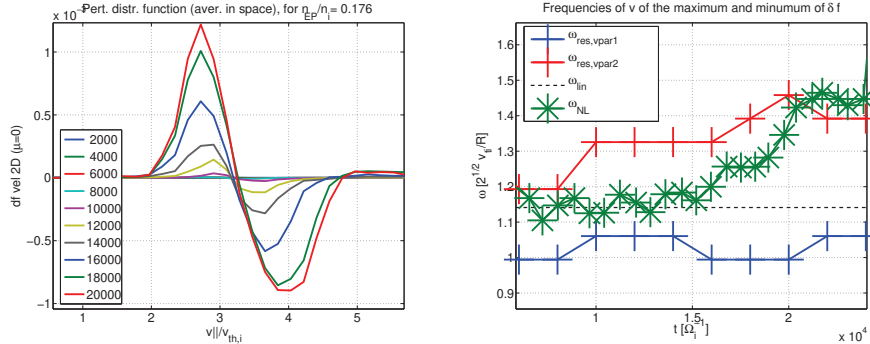
62

Figure 4.7: *Perturbed distr. funct. (left), for a case with $n_{EP}/n_i = 0.176$. The times are expressed here in units of Ω_i^{-1}. On the right, frequencies corresponding to the positive (red) and negative (blue) peaks of the EP perturbed distribution function. The measured EGAM freq. is also shown in green.*

is observed to grow in time, from $3.2\,v_{ti}$ to $3.5\,v_{ti}$.

The evolution of the resonance velocity in time is in relation with the EGAM nonlinear frequency modification, i.e. the EGAM chirping. The perturbed EP distribution function can be plotted explicitly (see Fig. 4.7-a). The positive peak (clump) and the negative peak (hole) can be seen to form and evolve in time, becoming bigger and centered at higher and higher distances from the linear resonance velocity. The location in velocity space of the peaks can be measured and translated into resonance frequencies as $\omega_{1,2} = v_{\|1,2}/qR$ (see Fig. 4.7-b). When compared with the measured EGAM frequency, we note that the nonlinear EGAM frequency modification at the time of the saturation is described with a good approximation by the resonance frequency of the negative peak (hole). This relation offers the possibility to predict the nonlinear frequency by approximating it with the frequency obtained by the velocity of the negative peak of the EP perturbed distribution function (see also Ref. [44]).

In the next section, Sec. 4.3.2, we introduce the beam-plasma instability (BPI) and the map linking the BPI with the EGAM. This map shows how we can predict the EGAM EP redistribution in velocity space.

4.3.2 Dynamics of the energetic particles: analogy with the beam-plasma instability

In general, the Langmuir wave can be decomposed in Fourier in terms of the wavenumbers $k_\ell = \ell(2\pi/L)$, where L is the periodicity length of the 1D space domain of the BPI, and ℓ is a positive integer (whereas the EGAM has only one possible wavenumber set by the equilibrium, as mentioned above). One can have two different regimes: (i) the one where several resonances are present in the unstable region of the phase space for which saturation is generally well described in the framework of the quasi-linear theory, and (ii) the one where there is a single mode in the unstable region, in which case saturation is due to particle trapping (wave-particle interaction). For the comparison described here, we refer to to situation (ii). Considering a single monochromatic wave with a chosen value of ℓ, we can focus on that, and we denote the wavenumber as k. The phase-angle Θ experienced by the electrons in the field of the Langmuir wave is thus $\Theta = kx - \omega_p t$ and the normalized variation in time of the phase angle is $\dot{\Theta}/\omega_p = k(v - v_r)/\omega_p = kv/\omega_p - 1$, where the resonant velocity is defined as $v_r = \omega_p/k$. As a choice of nomenclature, we refer in this subsection to the velocities of the EGAM as $v_\parallel$, and to the velocities of the BPI as v. Similarly, we refer to the wavenumbers of the EGAM as $k_\parallel = 1/qR$, and to the wavenumbers of the BPI as k.

In the following, we describe the detailed mapping procedure which links the EGAM framework with the BPI. As already mentioned, the dynamics of the EGAM model can be reduced in the parallel velocity direction and we start from the generic resonance condition written using two suitable normalization constants $\nu_{1,2}$, i.e.,

$$\frac{v_\parallel - v_{\parallel 0}}{\nu_1} = \frac{v - v_r}{\nu_2} \ , \tag{4.8}$$

where we recall that the transit resonance velocity reads $v_{\parallel res} = qR\omega_{EGAM}(n_{EP})$. Using the introduced above standard normalization $\nu_1 = v_{ti}$ and, for the calculation of this Section, $\bar{v}_\parallel = v_\parallel/v_{ti}$, in the following, we denote with $\bar{v}_{\parallel min} \leqslant \bar{v}_\parallel \leqslant \bar{v}_{\parallel max}$ the domain of the positive bump of energetic particles. Imposing the boundary $\bar{v}_{\parallel min} = 0 \ \mapsto \ v_{min} = 0$, in order to map one single bump of energetic particles with $\bar{v}_\parallel \geqslant 0$, we get $\nu_2 = v_r/\bar{v}_{\parallel r}$ and the map finally writes

$$v = \frac{v_r}{\bar{v}_{\parallel r}} \bar{v}_\parallel \ . \tag{4.9}$$

Let us now introduce the following normalization: $v = \omega_p(2\pi/L)^{-1} u$. In order to fix the dimensionless resonant wavenumber ℓ_r, we use the

condition $k_1 v_{max} = \omega_p$, with $v_{max} = v_r \bar{v}_{\|max}/\bar{v}_{\|r}$, which characterize the spectral features (wavenumbers and periodicity length). This yields $\ell_r = \ell_1 \bar{v}_{\|max}/\bar{v}_{\|r}$, and ℓ_r is determined arbitrarily fixing ℓ_1 since $\bar{v}_{\|max}$ and $\bar{v}_{\|r}$ are given quantities from the EGAM system. We stress how the resonance condition can be rewritten as $\ell_r u_r = 1$.

The map between the velocities of the two systems is now closed. The bump (positive part) of the EP is described by the shifted Maxwellian distribution function $F_{EP}(v_\|)$ in velocity space [67]. For modeling the EP distribution function of the EGAM in the BPI, let us now discretize the positive bump of $F_{EP}(v_\|)$ in n delta-like beams, equispaced in velocity space and located in $\bar{v}_{\|j}$ (with $j = 1, ..., n$), and assign the numbers of particles N_j for each beam distributed according to F_{EP}. The initial conditions on the distribution for BPI simulations are now given by N_j particles located at

$$u_j = \bar{v}_{\|j}/(\ell_r \bar{v}_{\|r}) \ . \tag{4.10}$$

For the sake of completeness, we mention that, for the simulation of the BPI, we have set $n = 600$, $\ell_1 = 400$ and we have used $N = 10^6$ total particles. The complete derivation of the BPI dynamical equation used here, is described in [68, 69] (and refs. therein), and it can be specified for one single resonance as:

$$\bar{x}_i' = u_i \, , \quad u_i' = i \, \ell_r \, \bar{\phi}_r \, e^{i\ell_r \bar{x}_i} + c.c. \, , \quad \bar{\phi}_r' = -i\bar{\phi}_r + \frac{i\eta}{2\ell_r^2 N} \sum_{i=1}^{N} e^{-i\ell_r \bar{x}_i} \, ,$$
$$\tag{4.11}$$

where the particle position along the x direction is labeled by x_i, with $i = 1, ... N$ (N being the total particle number) normalized as $\bar{x}_i = x_i(2\pi/L)$. The Langmuir electrostatic scalar potential $\phi(x,t)$ is expressed in terms of the Fourier component $\phi_r(k,t)$ and we have used: $\eta = n_B/n_p$ (for the plasma density n_p assumed much greater than the beam one n_B), $\tau = t\omega_p$ (the prime indicates derivative with respect to this variable), $\tilde{\phi}_r = (2\pi/L)^2 e\phi_r/m\omega_p^2$, $\bar{\phi}_r = \tilde{\phi}_r e^{-i\tau}$. Eqs. 4.11 are solved using a Runge-Kutta (fourth order) algorithm. For the considered time scales and for an integration step $h = 0.1$, both the total energy and momentum (for the explicit expressions, see [68]) are conserved with relative fluctuations of about 1.4×10^{-5}.

The BPI is closed once the density of the beam (drive) is fixed. In order to quantitatively compare the non-linear features of two systems, we now fix the bounce (trapping) frequency ω_B normalized to the mode frequency equal for the two schemes. For the BPI, the bounce frequency

results proportional to the linear growth rate of the mode $\gamma_{L,BPI}$. The same occurs for the EGAM system, but with a proportionality factor depending on the EP density [67]. In particular, we get:

$$\frac{\omega_{B,BPI}}{\omega_p} = \alpha \frac{\gamma_{L,BPI}}{\omega_p} \ , \qquad \frac{\omega_{B,EGAM}}{\omega_{L,EGAM}} = \beta(\bar{n}_{EP}) \frac{\gamma_{L,EGAM}}{\omega_{L,EGAM}} \ . \qquad (4.12)$$

where $\alpha \simeq 3.3$ (see well-known literature results [21, 104] and also [70]) while for the EGAM we have $\beta = \beta_0\sqrt{\omega_{L,EGAM}/\omega_{GAM}}$, with $\beta_0 = 2.66$ in this regime (see Sec. 3.3.1), and $\omega_{L,EGAM}$ depending on the EP density [67]. For the four selected EGAM simulations, we get $\beta(0.07, 0.10, 0.176, 0.30) \simeq$ [2.21, 2.17, 2.07, 1.98]. Using standard normalization for frequencies, i.e., $\bar{\gamma}_{L,BPI} = \gamma_{L,BPI}/\omega_p$ and $\bar{\gamma}_{L,EGAM} = \gamma_{L,EGAM}/\omega_{GAM}$, $\bar{\omega}_{L,EGAM} = \omega_{L,EGAM}/\omega_{GAM}$ and equaling the bounce frequencies, we finally get

$$\bar{\gamma}_{L,BPI} = \frac{\beta}{\alpha} \frac{\bar{\gamma}_{L,EGAM}}{\bar{\omega}_{L,EGAM}} \ . \qquad (4.13)$$

This condition preserves the linear and nonlinear features of the two systems and it is used in the evaluation for the drive of BPI simulations from the linear dispersion relation which formally reads as

$$\epsilon = 1 - \frac{\omega_p^2}{\omega^2} = \frac{\eta\omega_p^2}{k^2} \int_{-\infty}^{+\infty} dv \frac{k\,\partial_v \hat{F}_B(v)}{kv - \omega} \ . \qquad (4.14)$$

where $\hat{F}_B(v)$ is the initial beam distribution function. Here, the dielectric function ϵ can be expanded near $\omega \simeq \omega_p$ to deal with Langmuir modes as in Eqs. 4.11, i.e., $\epsilon \simeq 2(\bar{\omega} - 1)$ (where $\bar{\omega} = \omega/\omega_p$). Let us now use the expansion $\bar{\omega} = \bar{\omega}_0 + i\bar{\gamma}_{L,BPI}$, where $\bar{\omega}_0$ is the real part of the normalized Langmuir frequency $\bar{\omega}$. Using the linear character of the mapping which yields the normalization $\hat{F}_B(v) = \kappa F_{EP}(\bar{v}_\parallel)$ (with $\kappa = const.$), Eq. 4.14 can be written in terms of the EGAM system variables as

$$2(\bar{\omega}_0 + i\bar{\gamma}_{L,BPI} - 1) - \frac{\eta\bar{v}_{\parallel r}}{M} \int_{-\infty}^{+\infty} d\bar{v}_\parallel \frac{\partial_{\bar{v}_\parallel} F_{EP}}{\bar{v}_\parallel/\bar{v}_{\parallel r} - \bar{\omega}_0 - i\bar{\gamma}_{L,BPI}} = 0 \ , \qquad (4.15)$$

where $M = \int_{-\infty}^{+\infty} d\bar{v}_\parallel F_{EP}$. This equation is numerically integrated assuming Eq. 4.13, which guarantees the requested features described above, and provides the drive parameter η closing the map procedure.

4.3.3 Nonlinear transport in phase space, and comparison with the beam-plasma instability

In this section, we compare the results of the EP redistribution due to the EGAM, with the redistribution due to the beam-plasma instability.
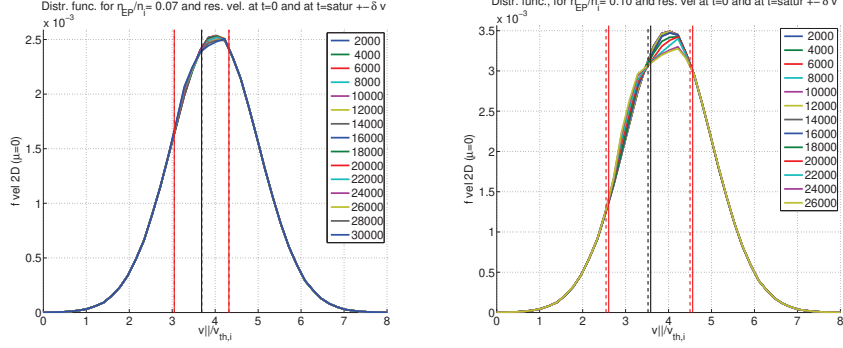
Figure 4.8: *Energetic particle distribution function averaged in space, and measured at $\mu \simeq 0$, vs parallel velocity, for $n_{EP}/n_i = 0.07$ (left) and $n_{EP}/n_i = 0.10$ (right). The vertical dashed and continuous lines are the resonance velocity (center), with the borders of the nonlinear velocity predicted by $v_{\parallel res} \pm \Delta v_{\parallel NL}$.*

In particular, we aim at predicting, from BPI informations, the nonlinear parallel velocity spread in the positive bump of the distribution function. The results shown here are discussed more in detail in Ref. [103].

In the BPI, the single mode dynamics proceeds in an initial exponential mode growth followed by non-linear saturation. Here the particles get trapped and begin to bounce back and forth in the potential well generating clumps. A measure of the clumps width Δu_{NL}^c for a generic
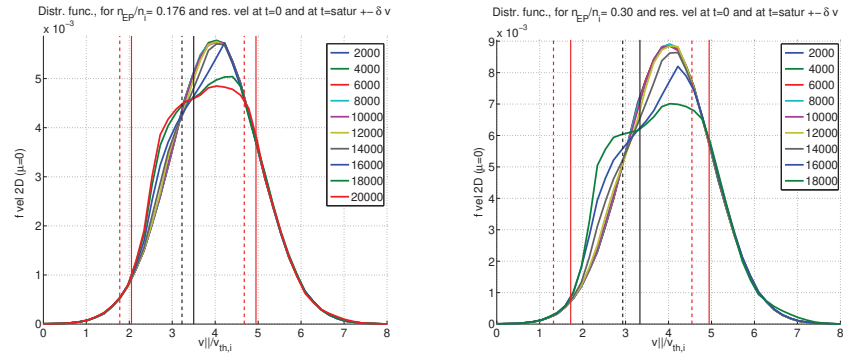

Figure 4.9: *Same as in Fig. 4.8 but for $n_{EP}/n_i = 0.176$ (left) and $n_{EP}/n_i = 0.30$ (right).*

initial half-Gaussian velocity distribution, which can be directly extrapolated to the analysis of the present work, has been evaluated in [70] for several cases outlining the following scaling rule as function of the linear drive:

$$\Delta u^c_{NL}/u_r = (6.64 \pm 0.12)\, \bar{\gamma}_L. \tag{4.16}$$

In order to include the dynamic role also of passing but nearly resonant particles, i.e. the region involved in the effective wave particle power exchange, in the following analysis we consider as the proper nonlinear particle velocity spread the scaled quantity $\Delta u_{NL} \simeq \chi \Delta u^c_{NL}$ with $\chi \simeq 1.28$. This estimate is derived [70] characterizing the active overlap of different non-linear fluctuations [105, 106] and corresponds to the finite distortion of the distribution function, including effects at the edges of the plateau (defined as the flattened region of the distribution function, mainly coinciding with the clump size). We finally obtain the desired formula for the prediction of the nonlinear velocity spread due to the EGAM:

$$\frac{\Delta v_{\parallel NL}}{v_{\parallel L,res}} = 8.5\, \bar{\gamma}_L^{BPI} \tag{4.17}$$

and by substituting the value of $\bar{\gamma}_L^{BPI}$ we obtain:

$$\frac{\Delta v_{\parallel NL}}{v_{\parallel L,res}} = 2.57\, \frac{\beta_0}{\sqrt{\omega_{GAM}}} \frac{\gamma_L^{EGAM}}{\sqrt{\omega_{L,EGAM}}} \tag{4.18}$$

Eq. 4.18 has been derived for the EGAM system, using the scaling derived in Eq. 4.13 and the normalized mapping of Eq. 4.10. For the regime of interest in this article, we have $\beta_0 = 2.66$ [67], and $\omega_{GAM} = 1.8\,\omega_s$, therefore we obtain:

$$\frac{\Delta v_{\parallel NL}}{v_{\parallel L,res}} = \frac{5.1}{\sqrt{\omega_s}} \frac{\gamma_L^{EGAM}}{\sqrt{\omega_{L,EGAM}}} \tag{4.19}$$

Let us now analyze the predictivity of Eq. 4.18, simplified as in Eq. 4.19 for the regime of interest. Four different simulations are considered, with different values of energetic particle concentration: $n_{EP}/n_i \in [0.07, 0.10, 0.176, 0.30]$. The corresponding linear frequencies and growth rates are $\omega_{L,EGAM} = [1.30, 1.24, 1.14, 1.04]\omega_s$ and $\gamma_{L,EGAM} = [0.04, 0.06, 0.09, 0.11]\omega_s$. In all simulations, the distribution function is averaged in space, and measured at $\mu \simeq 0$. Snapshots of the distribution function at different times are selected, going from the linear phase to the instant when the first peak of the electric field is reached, i.e. at saturation. In Fig. 4.8 and Fig. 4.9, the distribution functions measured with ORB5 are shown to
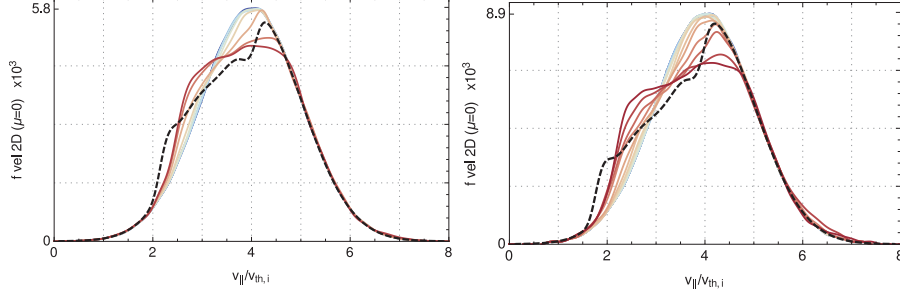
Figure 4.10: *Plot of the BPI distribution function taken at saturation time (dashed-black line) mapped back in the $v_\parallel$ space, over the evolution of the EP profile (color lines in standard color scheme from blue (t=2000 Ω_i^{-1}) to red (t=20000 Ω_i^{-1})) for $n_H/n_i = 0.17$ (left) and $n_H/n_i = 0.3$ (right).*

be modified by the nonlinear interaction with the EGAM, with a certain width in the velocity space. The position of the linear resonance velocity and the nonlinearly modified resonance velocity are shown for each simulation respectively as a dashed vertical black line, and a continuous vertical black line. We can now compare with the predicted values of Eq. 4.19: $\Delta v_{\parallel NL}/v_{\parallel L,res} = [0.17, 0.28, 0.45, 0.55]$. The corresponding predicted range is delimited by vertical red lines in Fig. 4.8 and Fig. 4.9. The dashed lines correspond to the range calculated with respect to the linear resonance velocity, and the continuous lines with respect to the nonlinearly modified resonance velocity. Note that the predicted width of the velocity domain of EP redistribution, centered at the nonlinearly modified resonance velocity, fits very well with the results of ORB5. Note also that, for the two cases with lowest drive, the nonlinear modification of the resonance velocity is negligible, and therefore the predicted width of the velocity domain of EP redistribution fits very well the results of ORB5, even when centered at the linear resonance velocity.

In summary, two distinct regimes can be identified. When the instabilities are weakly driven (Fig. 4.8), a very good match between the estimated deviation $v_{\parallel res} \pm \Delta v_{\parallel NL}$ and the nonlinear EP redistribution is observed, where $v_{\parallel res}$ is the linear resonance velocity. Otherwise, in the strongly driven regime (Fig. 4.9) the importance of the frequency chirping comes out. In particular, nonetheless the value $v_{\parallel res} \pm \Delta v_{\parallel NL}$ remains very predictive, as long as the nonlinearly modified resonance velocity is chosen as center of the EP redistribution due the EGAM.

69

The nonlinear frequency shift which is characteristic of the EGAM, can not be intrinsically implemented in the BPI model used here (although a chirping can be observed for different BPI models applied in other regimes, see for example Ref. [102]). The effect of this difference in the basic physics has effects on the EP redistribution. This clearly emerges in Fig. 4.10, where the distribution function of the BPI at saturation (dashed-black line), mapped back in the $v_\parallel$ space, is overplotted on the evolution of the EP profile for $n_{EP}/n_i = 0.176$ and $n_{EP}/n_i = 0.3$. In particular, it is evident how the discrepancy due the fixed character (at $\sim \omega_p$) of the Langmuir resonance gives rise to a very different morphology of the distribution function, although well predicting the effective nonlinear velocity spread. Also the inclusion of additional modes with artificial *ad hoc* damping rates results in a drastically non-comparable non-linear dynamics, underlining the intrinsic differences of the physical systems.

Chapter 5

Conclusions and outlook

The success of achieving magnetic-confinement nuclear fusion depends on the ability of controlling the stability and confinement of the energy and particles in the tokamak fuel: the hot plasma. Stability and confinement strongly depend on the presence or absence of plasma waves which can become unstable by tapping the plasma free energy, contained for example in the spatial gradients of the equilibrium temperature, or in the nonuniformity in phase space. Therefore, achieving a comprehensive theoretical model of the nonlinear dynamics of a tokamak plasma is important for understanding the plasma behavior in present-day tokamaks and predicting it in future reactors.

Among the different waves which are present in a tokamak plasma, we have focused here on low-frequency standing waves with acoustic polarization, named geodesic acoustic modes (GAMs). They can be excited by the nonlinear interaction with turbulence, or by the presence of an energetic particle (EP) population, via inverse Landau damping. In the latter case, these are called EP-driven GAMs, or also EP-induced GAMs (EGAMs).

In this dissertation, an overview of the recent development of our knowledge on the linear and nonlinear dynamics of EGAMs has been given. In particular, the results on the linear dynamics and on the wave-particle nonlinear dynamics of EGAMs, have been described. The main results described here have been obtained by A. Biancalani and by the PhD students I. Novikau and A. Di Siena under his supervision (with T. Görler acting as main internal advisor of A. Di Siena at the Max-Planck Institute for Plasma Physics in Garching, and E. Poli as academic advisor of I. Novikau and A. Di Siena at University of Ulm).

The linear dynamics of EGAMs has been investigated here in two kinds of magnetic equilibrium: analytical equilibria with circular flux sur-

faces, and equilibria taken from experimental reconstruction, with more general shape. Analytical equilibria with circular flux surfaces allow to focus on the main physics of the inverse Landau damping and compare with simple models for analytical theories. This comparison has been done for both GAMs and EGAMs. The effect of the flux surface elongation has been shown to modify the resonance position in phase space, consequently decreasing the growth rate, and also slightly modifying the frequency. A comparison with an ASDEX Upgrade selected case, the so-called NLED-AUG base case, has shown how a good agreement of the linear frequency obtained with numerical simulations and the onset of the nonlinear frequency chirping cycle can be found, despite the approximations in the EP distribution function and the adiabatic model for the electrons. When including kinetic electron effects, the growth rate of the NLED-AUG case has been found to decrease, due to a higher damping, given by the electron Landau damping, and to a modified frequency and mode structure, which indirectly affects the ion Landau damping. A mode particle resonance diagnostics has shown how the dominant electrons responsible for this, are the barely trapped electrons.

The nonlinear dynamics of EGAMs has also been studied, focusing on the wave-particle nonlinearity, i.e. the nonlinearity responsible for the redistribution of the EP population in phase space. For this investigation, the comparison with the beam-plasma instability (BPI) has been of crucial importance. In fact, due to the 1-1 analogy which has been created here, a reduced model has been constructed, capable to predict saturation levels and the amount of redistributed EP in phase space, due to the EGAM. Regarding the EP redistribution, two regimes have been identified: the regime where the EGAMs are weakly driven shows a very good match between the nonlinear EP redistribution observed in the two problems; on the other hand, above a certain threshold in the drive, a difference is found. The difference has been shown to occur due to the nonlinear modification of the mode frequency (i.e. the frequency chirping) which exists for the EGAMs, but is not observed for the BPI with the adopted model, for the cases of interest. It is important to note that the scaling of the saturated electric field with the linear growth rate was found to be quadratic in Ref. [67], and it does not change at the threshold of the two regimes identified here. Therefore, we have stated that the onset of a non-negligible frequency chirping affects the EP redistribution in velocity space but not the scaling of the saturated levels. The EP redistribution of the EGAM has been shown to be recovered with the BPI in the high-drive regime, by adding an ad-hoc frequency modification to the BPI model. As main results, the formulas for the predictions of the

nonlinear saturation level and width of the velocity redistribution around the resonance velocity have been provided.

The study of the nonlinear saturation of EGAMs due to wave-wave interaction is in progress, and constitutes one of the topics of the next publications. Wave-wave coupling of an EGAM with itself, and of an EGAM with turbulence, is under consideration. Moreover, experimental observations like the NLED-AUG case show how EGAMs coexist with Alfvénic activity, and therefore more complex nonlinear couplings can occur. These would be responsible for different redistribution of the EP population, and therefore are necessary to study for achieving a comprehensive understanding of the global nonlinear behavior of EGAMs in tokamak plasmas, and eventually constructing a selfconsistent model for the stability and transport of turbulent burning plasmas in fusion devices.

Acknowledgments

Bibliography

[1] ITER Research Plan within the Staged Approach, https://www.iter.org/technical-reports

[2] B. D. Scott, *Plasma Phys. Control. Fusion* **49**, S25-S41 (2007)

[3] N. Winsor et al. *Phys. Fluids* **11**, 2448, (1968)

[4] F. Zonca and L. Chen, *Europhys. Lett.* **83**, 35001 (2008)

[5] G. D. Conway, et al, *Nucl. Fusion* **50**, 055009 (2008)

[6] Z. Qiu, L. Chen and F. Zonca, *Plasma Science and Tech.* **20**, 094004 (2018)

[7] M.N. Rosenbluth and F.L. Hinton, *Phys. Rev. Lett.* **80**,4 724 (1998)

[8] P. H. Diamond, S.-I. Itoh, K. Itoh, and T. S. Hahm, *Plasma Phys. Control. Fusion* **47** 5, R35R161 (2005)

[9] G. D. Conway, et al., *Phys. Rev. Lett.* **106**, 065001 (2011)

[10] Z. Lin, T. S. Hahm, W. W. Lee, W. M. Tang, and R. B. White, *Science* **281**, 1835 (1998)

[11] F. Palermo, A. Biancalani, et al., *Europhys. Lett.* **115**, 15001 (2016)

[12] A. Biancalani, et al., *Phys. Plasmas* **23**, 112115 (2016)

[13] I. Novikau, A. Biancalani, A. Bottino, G. D. Conway, Ö. D. Gürcan, P. Manz, P. Morel, E. Poli, A. Di Siena, the ASDEX Upgrade Team, *Phys. Plasmas* **24**, 122117 (2017)

[14] G. Fu, et al., *Phys. Rev. Lett.* **101**, 185002 (2008)

[15] L. I. Rudakov and R. Z. Sagdeev, *Sov. Phys. Dokl.* **6** 498 (1965)

[16] A. Bottino, et al. *Plasma Phys. Control. Fusion* **53**, 124027 (2011)

[17] A. Biancalani, et al., *25th IAEA Fusion Energy Conference, Saint Petersburg, Russia*, 13-18 October 2014.

[18] A. Biancalani, et al, *45th EPS Conference on Plasma Physics* 2-6 July 2018, P2.1003

[19] A. Biancalani, et al., *27th IAEA Fusion Energy Conference, Ahmedabad, India*, 22-27 October 2018, TH/P2-9 https://conferences.iaea.org/indico/event/151/contributions/6036/

[20] F. Carpanese, A. Biancalani, et al, "Using IPF-FDMC full-wave code as a synthetic reflectometer for studying micro-instabilities computed by ORB5", DPG conference, Hannover, 2016

[21] L. Chen and F. Zonca, *Rev. Mod. Phys.* **88**, 015008 (2016)

[22] L. Chen and A. Hasegawa, *Phys. Fluids* **17** 1399 (1974)

[23] C. E. Kieras and J. A. Tataronis, *J. Plasma Physics* **28**, 395 (1982)

[24] C. Z. Cheng, et al., *Ann. Phys.* **161**, 21 (1985).

[25] A. Biancalani, et al., *26th IAEA Fusion Energy Conference, Kyoto, Japan*, 17-22 October, 2016 (ORAL), https://conferences.iaea.org/indico/event/98/session/26/contribution/457

[26] A. Biancalani, et al., *Phys. Plasmas* **23**, 012108 (2016)

[27] M. Cole, A. Biancalani, et al., *Phys. Plasmas* **24**, 022508 (2016)

[28] A. Biancalani, et al., *Plasma Phys. Control. Fusion* **59**, 054004 (2017)

[29] M. S. Chu *et al. Phys. Fluids B* **4** 3713 (1992)

[30] F. Zonca, L. Chen and R.A. Santoro *Plasma Phys. Control. Fusion* **38**, 2011-2028 (1996)

[31] P. Buratti, et al., *Nuclear Fusion* **45** 1446 (2005)

[32] A. Botrugno, A. Biancalani, et al., *37th EPS Conference, Dublin, Ireland* (2010)

[33] C. Wei, et al. *Journal of the Phys. Soc. Japan* **79** 044501 (2010)

[34] A. Biancalani, *PhD thesis*, University of Pisa, Italy (2010).

[35] A. Biancalani, L. Chen, F. Pegoraro and F. Zonca, *Phys. Rev. Lett.* **105**, 095002 (2010).

[36] A. Biancalani, L. Chen, F. Pegoraro and F. Zonca, *Phys. Plasmas* **17**, 122106 (2010).

[37] A. Biancalani, L. Chen, F. Pegoraro and F. Zonca, *Plasma Phys. Control. Fusion* **53** 025009 (2010) arXiv:1009.1556.

[38] A. Biancalani, L. Chen, F. Pegoraro, F. Zonca, S.V. Annibaldi, A.Botrugno, P. Buratti and P. Smeulders, *22nd IAEA Fusion Energy Conference, 13-18 October, Geneva* Poster Th/P3-5 (2008), http://www-pub.iaea.org/MTCD/Meetings/fec2008pp.asp

[39] A. Tuccillo, A. Biancalani, et al. *Nucl. Fusion* **49** 104013 (2009)

[40] A. Hasegawa, C. G. Maclennan, and Y. Kodama, *Phys. Fluids* **22**, 2122 (1979)

[41] H. L. Berk, et al., *Nucl. Fusion* **46**, S888S897 (2006)

[42] Z. Qiu, F. Zonca, and L. Chen *Plasma Phys. Control. Fusion* **52** (9), 095003 (2010)

[43] Z. Qiu, F. Zonca, and L. Chen *Plasma Sci. Technol.* **13** (3), 257 (2011)

[44] H. Wang, Y. Todo, and C. C. Kim, *Phys. Rev. Lett.* **110** (15), 155006 (2013)

[45] D. Zarzoso et al.*Phys. Rev. Lett.* **110**, 125002 (2013)

[46] K. Miki, and Y. Idomura *Plasma Fusion Res.* **10**, 3403068 (2015)

[47] D. Zarzoso et al. *Nucl. Fusion* **57** (7), 072011 (2017)

[48] M. Sasaki, et al. *Scientific Rep.* **7**, 16767 (2017)

[49] A. Di Siena, A. Biancalani, T. Görler, H. Doerk, I. Novikau, P. Lauber, A. Bottino, E. Poli, and the ASDEX Upgrade Team, *Nucl. Fusion* **58**, 106014 (2018)

[50] R. Nazikian, et al., *Phys. Rev. Lett.* **101**, 185001 (2008)

[51] L. Horváth, et al, *Nucl. Fusion* **56** (11), 112003 (2016)

[52] D. Zarzoso et al. *Nucl. Fusion* **58**, 106030 (2018)

[53] H.S. Zhang and Z. Lin *Phys. Plasmas* **17**, 072502 (2010)

[54] K. Hallatscheck *Phys. Rev. Letters* **93**, 12, 125001, (2004)

[55] B. D. Scott *New Journ. of Phys.* **7** 92 (2005)

[56] R. Hager and K. Hallatschek *Phys. of Plasmas* **16** 072503 (2009)

[57] H. Sugama and T.H. Watanabe, *J. Plasma Physics* **72**, 825 (2006)

[58] H. Sugama and T.H. Watanabe, *J. Plasma Physics* **74**, 139 (2008)

[59] Z. Qiu, L. Chen and F. Zonca, *Plasma Phys. Control. Fusion* **51** 012001 (2009)

[60] T. O'Neil, *Phys. Fluids* **8**, 22552262 (1965)

[61] T. M. O'Neil and J. H. Malmberg *Phys. Fluids* **11**, 17541760 (1968)

[62] M. Lesur, et al. *Phys. Rev. Lett.* **116** (1), 015003 (2016)

[63] D. Zarzoso, et al., *Phys. Plasmas* **19** 022102-1 (2012)

[64] D. Zarzoso, A. Biancalani, et al., *Nucl. Fusion* **54** 103006 (2014)

[65] Z. Qiu, I. Chavdarovski, A. Biancalani, and J. Cao, *Phys. Plasmas* **24**, 072509 (2017)

[66] M. B. Levin, et al. *Sov. J. Exp. Theor. Phys.* **35**, 898 (1972)

[67] A. Biancalani, I. Chavdarovski, Z. Qiu, A. Bottino, D. Del Sarto, A. Ghizzo, Ö. Gürcan, P. Morel, I. Novikau, *J. Plasma Phys.* **83** 6, 725830602 (2017)

[68] N. Carlevaro, et al. *J. Plasma Phys.* **81** (5), 495810515 (2015)

[69] N. Carlevaro, et al. *Entropy* **18**, 143 (2016)

[70] N. Carlevaro, et al. *45th EPS Conference on Plasma Physics* P5.1067 (2018)

[71] T. M. Antonsen and B. Lane, *Phys. Fluids* **23**, 1205 (1980)

[72] E. A. Frieman and L. Chen, *Phys. Fluids* **25**, 502 (1982)

[73] R. G. Littlejohn, *J. Plasma Phys.* **29**, 111 (1983)

[74] T. S. Hahm, W. W. Lee, and A. Brizard, *Phys. Fluids* **31**, 1940 (1988)

[75] A. Brizard, *J. Plasma Phys.* **41**, 541 (1989)

[76] H. Sugama, *Phys. Plasmas* **7**, 466 (2000)

[77] A. J. Brizard and T. S. Hahm, *Rev. Mod. Phys* **79**, 421 (2007)

[78] C. K. Birsdall, A. B. Langdon, "Plasma Physics via computer simulations", Adam Hilger, Bristol (1989)

[79] W. W. Lee, *Phys. Fluids* **26**, 556562 (1983)

[80] F. Jenko, W. Dorland, M. Kotschenreuther, and B. N. Rogers, *Phys. Plasmas* **7**, 1904 (2000)

[81] A. Biancalani, et al., *Phys. Plasmas* **24**, 062512 (2017)

[82] A.M. Dimits et al., *Phys. of Plasmas* **7** 969 (2000)

[83] G. Falchetto et al., *Phys. Plasmas* **50** 124015 (2008)

[84] A. Mishchenko, et al., *Phys. Plasmas* **15** 112106 (2008)

[85] S. Jolliet, et al. *Comput. Phys* **177**, 409 (2007)

[86] V. Grandgirard et al. *Commun. Nonlinear Sci. Numer. Simul.*, **13** 81 (2008)

[87] Y. Sarazin et al. *Nucl. Fusion* **50**, 054004 (2010)

[88] A. Bottino and E. Sonnendrücker, *J. Plasma Phys.* **81**, 435810501 (2015)

[89] L. Chen, *Phys. of Plasmas* **1**, 1519 (1994)

[90] A. Biancalani, et al, *Nucl. Fusion* **54**, 104004 (2014)

[91] Ph. Lauber, S. Günter, A. Könis, S.D. Pinches, *Journal of Comp. Phys.* **226**, 447 (2007)

[92] I. Novikau, A. Biancalani, A. Bottino, A. Di Siena, P. Lauber, E. Poli, E. Lanti, L. Villard, N. Ohana, S. Briguglio, "Implementation of energy transfer technique in ORB5 to study collisionless wave-particle interactions in phase-space" *submitted to Comp. Phys. Comm.* (2019) arxiv:1903.05024

[93] T. Görler, X. Lapillonne, S. Brunner, T. Dannert, F. Jenko, F. Merz, and D. Told, *J. Comput. Phys.* **230**, 7053 (2011)

[94] V. Grandgirard, et al. *Comput. Phys. Commun.* **207** 35-68 (2016)

[95] D. Estève, et al., *Phys. Plasmas* **22**, 122506 (2015)

[96] E. Sonnendrücker, J. Roche, P. Bertrand, A. Ghizzo, *J. Comput. Phys.* **149** (2) 201220 (1999)

[97] V. Grandgirard, et al., *J. Comput. Phys.* **217**-2 395423 (2006)

[98] P. Lauber, NLED-AUG case description, `http://www2.ipp.mpg.de/~pwl/NLED_AUG/data.html`

[99] A. Mishchenko, A. Bottino, R. Hatzky, E. Sonnendrücker, R. Kleiber, A. Könies *Phys. Plasmas* **24** (8), 081206 (2017).

[100] Y. Chen, S. Parker, *Phys. Plasmas* **8** (5), 2095-2100 (2001)

[101] R. Hatzky, A. Könies, A. Mishchenko *J. Comp. Phys.* **225** (1), 568-590 (2007)

[102] M. Lesur, Y. Idomura, and X. Garbet *Phys. Plasmas* **16** (9), 092305 (2009)

[103] A. Biancalani, et al., *J. Plasma Phys.* **84**, 725840602 (2018).

[104] Y. Wu et al., *Phys. Plasmas* **2**, 4555 (1995)

[105] D.F. Escande, F. Doveil, *J. Stat. Phys.* **26**, 257 (1981)

[106] A.J. Lichtenberg and M.A. Lieberman, *Regular and Chaotic Dynamics - Second Edition* (Springer-Verlag) (2010)

[107] Z. Gao, L. Peng, P. Wang, J. Dong, and H. Sanuki, *Nucl. Fusion* **49** 045014 (2009)

[108] Z. Gao, *Phys. Plasmas* **17**, 092503 (2010)